이학박사 학위논문

Investigation on strain-induced anomalous magnetotransport in antiferromagnetic pyrochlore iridate thin films

반강자성 파이로클로어 이리듐 박막에서 변형유도 이상 자기수송에 관한 조사

2023 년 8 월

서울대학교 대학원

물리천문학부

송정근

Investigation on strain-induced anomalous magnetotransport in antiferromagnetic pyrochlore iridate thin films

Jeongkeun Song

Supervised by

Professor Changyoung Kim

A Dissertation Submitted to the Faculty of Seoul National University in Partial Fulfillment of the Requirements for the Degree of Doctor of Philosophy

August 2023

Department of Physics and Astronomy

Graduate School

Seoul National University

Investigation on strain-induced anomalous magnetotransport in antiferromagnetic pyrochlore iridate thin films

반강자성 파이로클로어 이리듐 박막에서 변형 유도
이상자기수송에 관한 조사

지도교수 김창영

이 논문을 이학박사학위논문으로 제출함
2023 년 6 월

서울대학교 대학원
물리·천문학부
송정근

송정근의 박사학위논문을 인준함
2023 년 6 월

위 원 장 **차국린** (인)

부 위 원 장 **김창영** (인)

위 원 **노태원** (인)

위 원 **양범정** (인)

위 원 **손창희** (인)

Contents

Abstract

Searching for quantum materials with nontrivial band topology has been one of the central themes in the field of both materials science and condensed matter physics. The family of 5*d* pyrochlore iridates ($R_2Ir_2O_7$, *R* = rare earth ions) has gained significant interest due to the interplay between comparable strength of the parameters such as the Coulomb interaction (*U*) and spin-orbit coupling (λ). This interplay is predicted to result in a fertile topological state of matter, including a topological insulator, Weyl semimetallic state, and axion insulator.

$R_2Ir_2O_7$ thin films offer a suitable platform for investigating topological phases and exotic phenomena hidden in bulk due to cubic crystalline symmetry. The epitaxial strain can break cubic crystalline symmetry, providing practical tunability to access hidden topological phases. Despite the extensive interest, the fabrication of high-quality single-crystalline (111) $R_2Ir_2O_7$ thin films remains challenging due to the formation of highly volatile gaseous iridium oxides (IrO_3) during growth. The vast majority of successfully grown $R_2Ir_2O_7$ thin films have been realized via the two-step protocol called "solid phase epitaxy (SPE)." However, the SPE method produces either relaxed or partially-strained $R_2Ir_2O_7$ films, which is not ideal for investigating strain-induced topological phenomena. In this thesis, I will discuss the new growth method for fabricating strained $Nd_2Ir_2O_7$ (NIO-227) thin films, the way to optimize and utilize the new growth method, and strain-induced magnetotransport phenomena in strained NIO-227 films.

Keywords: Topological phases, pyrochlore iridate, epitaxial strain, new growth method, magnetotransport.

Student number: 2017-26221

List of Figures

RRHSE method is the ablation of the IrO2 target. The additional ablation of the IrO2 target compensates for the severe Ir loss during the deposition of NIO-227 film. (c) The third step of the RRHSE method is the rapid thermal annealing of the sam- ple from steps (a) and (b) at high T to form the pyrochlore phase, with a rapid temperature increase of 400°C/min to 850°C. (d) After annealing the sample, the steps in (a)–(c) are repeated to achieve the desired thickness of films. Adapt from[23].

Figure 3.1 X-ray diffraction of NIO-227 films grown with different amounts of IrO_2 ablation (> 70 %). (a) X-ray diffraction (XRD) θ-2θ scans of NIO-227 films with different amounts of IrO_2 ablation ranging from 80 to 100 %. Films grown with 85 % IrO_2 ablation show strong NIO-227 signals, while films grown with 80 % IrO_2 ablation results in an off-stoichiometric sample. The asterisks (*) mark the YSZ substrate (111) and (222) peaks. YSZ Panel (b) provides a magnified view of the XRD patterns from (a), with the black dashed line indicating the position of the bulk NIO-227 (444) peak. (c) Reciprocal space map of the films grown with 80 % and 90 % IrO_2 ablation in the vicinity of the YSZ (331) reflection. The dashed lines present the peak position of the films. (d) By Bragg's law, the calculated *c* - lattice constant of all samples from the peaks near YSZ (222) is shown. The dashed line presents the position of the bulk NIO-227 (444).

Figure 3.2 X-ray diffraction of NIO-227 films grown with different amounts of IrO_2 ablation. X-ray diffraction (XRD) $\theta-2\theta$ scans of NIO-227 films with varying amounts of IrO_2 ablation (0 ~ 40 and 100 %).

Figure 3.3 Cross-sectional scanning transmission electron microscopy images of films. High-angle annular dark field scanning transmission electron microscopy (HAADF-STEM) images of NIO-227 film grown with (a) 80 % IrO_2 ablation and (b) with 90 % IrO_2 ablation. The image

of the NIO-227 film grown with 80 % IrO_2 ablation reveals inhomogeneity, with a cloudy region near the interface (highlighted in red). On the other hand, the image of the NIO-227 films grown with 90 % IrO_2 ablation shows homogeneity and high-quality.

Figure 3.4 Intrinsic magnetotransport properties of the films with different amounts of IrO_2 ablation (> 70%) (a) The plot of the longitudinal resistivity, ρ_{xx}, vs. temperature, T, of NIO-227 films grown above 75 %. The schematic image shows the measurement direction where the current is applied [110] direction. (b) Anomalous Hall effects (AHE) measurement is performed with an external magnetic field (H_{ext}) applied along the [111] direction and current (I) flowing along the [110] direction at 2 K. (c) The log plot of σ_{xy}^{AHE} vs. σ_{xx} for strained NIO-227 thin films with different amounts of IrO_2 ablation at H_{ext} = 0 T. The straight red dotted line features the $\sigma_{xx}^{1.6}$ dependence of σ_{xy}^{AHE}, indicating the intrinsic origin of σ_{xy}^{AHE}.

Figure 4.1 Schematic diagram of strain-induced cluster magnetic multipoles and OM in $Nd_2Ir_2O_7$ thin films. a. Schematic view of the pyrochlore lattice structure of $Nd_2Ir_2O_7$. b. When compressive strain is applied to $Nd_2Ir_2O_7$ along the [111] direction, the AIAO configuration of the magnetic spin experiences spin canting. Such canting can be represented by three distinctive magnetic multipoles (dipole, A_2-octupole, and T_1-octupole). Note that the dipole has finite magnetization, whereas the A_2-octupole and T_1-octupole do not have magnetization. c. Schematic diagram of the longitudinal magnetization induced by the dipole. When H_{ext} is applied along the x-y plane, the spin direction is aligned in the direction of H_{ext}. d. Schematic diagram of the OM induced by coupling between an external magnetic field (H_{ext}) and magnetic octupoles. The OM can be induced in two directions: normal to the surface and in-plane.

Figure. 4.2 Characterization of a $Nd_2Ir_2O_7$ thin film. a. High-resolution XRD pattern of a 15 nm thick $Nd_2Ir_2O_7$ (NIO-227) thin film. The NIO-227 thin film was grown on a YSZ substrate. b. Reciprocal space map of the NIO-227 film in the vicinity of the YSZ (331) reflection,

indicating that the NIO-227 film is fully strained. c. The plot of the longitudinal resistivity, ρ_{xx}, vs. temperature, *T*, of NIO-227 thin film and single crystal (Ref. 46 in the main manuscript). d. The AHE is measured by applying H_{ext} along the [111] direction and *I* along the $[1\bar{1}0]$ direction at 2 K. A clear AHE without a magnetic field is the signature of the presence of the T_1-octupole in the NIO-227 thin film.

Figure. 4.3 Anomalous magnetic oscillation in the $\Delta\sigma_{xy}^{PHE}(\phi,\ H\ = \pm 9\ \mathrm{T})$ of the NIO-227 thin film. a. Schematic diagram of the $\Delta\ \sigma_{xy}^{PHE}(\phi)$ measurement geometry. In this geometry, *I* is applied along the $[1\ \bar{1}\ 0]$ direction and H_{ext} is rotated within the sample plane. b. $\Delta\ \sigma_{xy}^{PHE}(\phi)$ curves at 20 and 2 K. At 20 K, the $\Delta\ \sigma_{xy}^{PHE}(\phi)$ curve has a sin (2ϕ) oscillation. c. Contour plot of all $\Delta\ \sigma_{xy}^{PHE}(\phi)$ curves below 30 K. d. FFT results of all $\Delta\ \sigma_{xy}^{PHE}(\phi)$ curves with different *T*. The FFT intensities of the second, fourth, and sixth harmonics are related to magnetization from the dipole, OM induced by the A_2-CMO, and OM induced by the T_1-CMO, respectively. The inset shows the temperature dependence of the sixth harmonic below 30 K.

Figure 4.4 Process of fast Fourier transform of planar Hall effect curves. To see the dependency on each harmonic in the planar Hall effect curves, the fast Fourier transform was performed. a. The T ~ 2 K data of the planar Hall effect are shown to demonstrate the process of performing fast Fourier transforms in this work. b. The plot of the planar Hall effect was converted into radians. c. The plot of the performed fast Fourier transform.

Figure 4.5 Nonlinear magnetic behavior of the $\Delta\sigma_{xy}^{PHE}(\phi\ =\ 45°, \mathrm{H})$ of the NIO-227 thin film. a. Schematic diagram of the $\Delta\sigma_{xy}^{PHE}(H)$ measurement geometry. b. $\Delta\sigma_{xy}^{PHE}(H)$ curves as a function of H_{ext} below T ~20 K. In the region of 15 K < T < 20 K, the value of $\Delta\sigma_{xy}^{PHE}(H)$is nearly zero. The slight deviation of $\Delta\sigma_{xy}^{PHE}(H)$ near $H_{ext} \sim \pm 9\ T$ at T ~15 K is possibly due to dipolar order. c. Logarithmic plot of the results of fitting $\Delta\ \sigma_{xy}^{PHE}(H)$ at T ~ 4 K with

$\Delta\sigma_{xy}^{PHE}(H) = a_2H^2 + a_3H^3 + a_4H^4$ (red line). d. The plot of extracted fitting parameters a_2, a_3, and a_4 and $\Delta\sigma_{xy}^{PHE}(H = 9\ T)$ for the measured T.

Table 1 Contributions of magnetic orderings to the anomalous and planar Hall effects. Each contribution of magnetic orderings to the anomalous and planar Hall effects is shown. The contribution of T_1-octupole ordering to the σ_{xy}^{AHE}(H) of the $Nd_2Ir_2O_7$ thin film can induce a finite $\sigma_{xy}^{AHE}(H = 0)$[2]. In contrast, the orthogonal magnetization, $M_\perp$, is induced from cluster magnetic octupoles, affecting $\sigma_{xy}^{PHE}(\phi)$ and σ_{xy}^{PHE}(H) with distinctive features.

Figure 4.6 The emergence of T_1-octupole under strain and magnetic field. We present A_2-octupole and T_1-octupoles under the change of strain and magnetic field. The blue solid line is A_2, the orange dotted line is T_{1x}, the orange circles are T_{1y}, and the orange solid line is T_{1z}. a. The change of order parameters when the strain δ varies from 0 to 0.01 with $\vec{B} = 0$. When the strain is absent ($\delta = 0$), only A_2-octupole exists. When $\delta \neq 0$, only T_{1z} emerges linearly to δ while T_{1x} and T_{1y} remains trivial. b. The change of order parameters when magnetic field strength varies from 0 to 0.02 with $\phi = 0, \delta = 0.005$. T_{1x} emerges linearly to δ, and other order parameters change quadratically to δ. c. The change of magnetization when the strain δ varies from 0 to 0.01 with $\vec{B} = 0$. d. The change of magnetization when magnetic field strength varies from 0 to 0.02 with $\phi = 0, \delta = 0.005$.

Figure 4.7 The angular dependence of A_2 and T_1-octupoles. We present the change of order parameters for two cases. a-b. $\vec{B}$ is in the [111] plane. ϕ varies from 0 to 2π, with $\delta = 0.005, U = 1.485\ t_{oxy}$, and $B = 0.02$. a. A_2-octupole (blue solid line) and T_{1z}-octupole (orange solid line) which are proportional to $sin\ 3\phi$. b. T_{1x} (orange dotted line) and T_{1y} (orange circles) which are proportional to $cos\ \phi$ and $sin\ \phi$, respectively. c-d. $\vec{B}$ is in the $[11\bar{2}]$ plane. θ varies from 0 to 2π, with $\delta = 0.01, U = 1.5\ t_{oxy}$, and $B = 0.02$. c. A_2-octupole (blue solid

line) and T_{1z}-octupole (orange solid line) are proportional to $sin\,3\theta$. d. T_{1x} (orange dotted line) and 30 times T_{1y} (orange circles) which are proportional to $cos\,\theta$ and $cos\,2\theta$, respectively. The schematics of the physical geometry when e. $\vec{B}$ in the [111] plane and f. $\vec{B}$ in the $[11\bar{2}]$ plane.

Figure 4.8 Plot of the calculated PHC below 30 K and their fitting results.

Figure 4.9 Anisotropic magnetoconductance and fitting with cluster multipoles contributions. σ_{AMR} (ϕ) measured at a. 2 K, b. 4 K, c. 6 K, d. 8 K, e. 10 K, f. 12 K, g. 15 K, h. 20, and i. 30 K. The black line is experimental data while the red line is the fitting result with theoretical AMR equation.

Figure 4.10 Temperature dependence of out-of-plane rotation magnetoconductivities. a. Schematic of out-of-plane rotation measurement. The current is applied along $[1\bar{1}0]$ direction and magnetic field is rotated along [111] and [1 $\bar{1}$ 0] plane. b. Experimental magnetoconductivities below 15 K and their fitting.

Chapter 1
Introduction

1.1 Novel correlated topological phases in 5*d* transition metal oxides

The discovery of topological insulators ignited the intensive theoretical and experimental investigation of topological states of matter. Such intensive efforts have delivered the "Zoo" of topological materials. In the Zoo, the symmetry-protected topological phases exist with unique quantum mechanical wavefunction. Each phase possesses an exotic surface state and quantized transport phenomena. Also, these exotic properties of topological materials can be utilized to build quantum sensing and thermoelectric devices.

On the other hand, there has been a recent shift in the research paradigm to search for materials with emergent quantum phenomena. By combining two energy scales (electron correlation and spin-orbit coupling), novel topological phases with novel functionalities can arise. These phases are classified as correlated topological phases (CTPs), including Weyl and nodal line semimetals, Axion insulators, and topological Mott insulators[1] (Fig. 1.1). The main attractiveness of CTPs is that topological order can emerge purely as a result of correlations within a solid. As a consequence, the correlated topological materials exhibit unusual quantum phenomena such as anomalous Hall effect without magnetization, chiral anomaly, and superconductivity.

Transition metal oxides have attracted enormous attention because of their electronic and magnetic properties such as high-temperature superconductivity, colossal magnetoresistance, and multiferroics. Decades of research have found that these exotic phenomena in 3*d*/4*d* oxides originate from the strong correlation between the degrees of

freedom such as charge, spin, and orbital. These understandings enabled the technological advances in epitaxial growth of complex oxides that equaling or surpassing functionalities to those of bulk system. On the other hand, comparing with 3*d* and 4*d* state, the 5*d* compounds can have richer quantum states and functionalities. Owing strong spin-orbit coupling due to large atomic number, the various anomalous quantum state can arise, including quantum spin liquid and topological insulator. Furthermore, the interplay between degrees of freedom and spin-orbit coupling can resulted into emergence of CTPs.

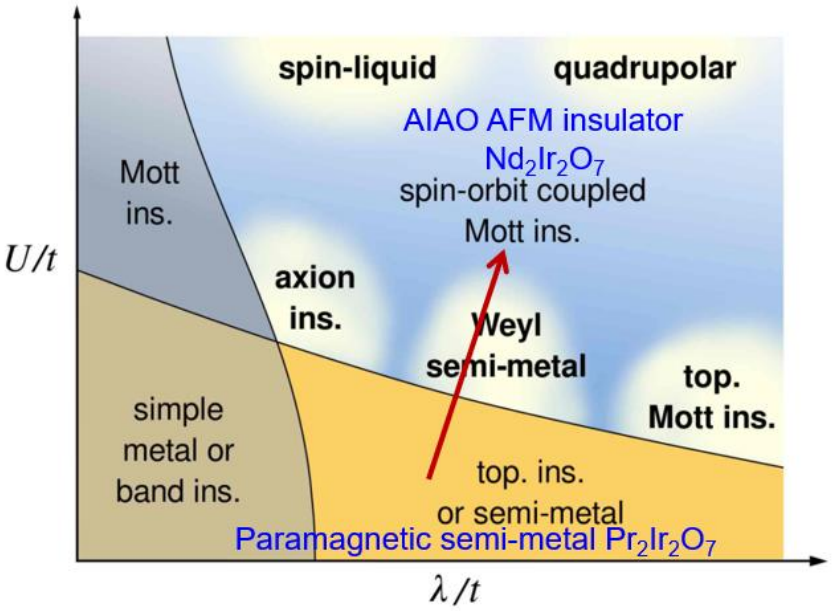

Figure 3.1 Phase diagram of novel topological phase diagram. Adapted from[1]

1.2 5*d* pyrochlore iridate

Among the handful of candidates, the family of 5*d* pyrochlore iridate ($R_2Ir_2O_7$, R = rare earth ions) received tremendous attention. Initially, the family of 5*d* pyrochlore iridate is the first theoretical real materials system that can host Weyl fermions in electronic structure[2]. Within a few years after the first theoretical prediction, vast CTPs are theoretically [2-5] to emerge by the interplay between similar strength of electron correlation (*U*), spin-orbit coupling (*SOC*), and hopping parameters. Pyrochlore iridates have a cubic pyrochlore crystallographic structure (Fig. 1(a)). Most bulk $R_2Ir_2O_7$ compounds exhibit intriguing antiferromagnetic spin ordering, namely all-in-all-out (AIAO) ordering[6] where the magnetic moments at all four corners of one (neighboring) tetrahedron point inward (outward) (Fig. 1.2 (b)). This intriguing magnetic ordering naturally breaks the time-reversal symmetry and preserves the inversion symmetry of its fourfold degenerate Fermi nodes, and meets the criteria for realizing a magnetic WSM state[1]. In addition, numerous other correlated topological phases such as topological insulator[3], axion insulator[4], and nodal semimetal[5] have been proposed.

Compared to detailed theoretical studies, experimental studies on $R_2Ir_2O_7$ have been limited to bulk systems. Experimental results on bulk $R_2Ir_2O_7$ showed that its electronic ground state changes from a metal to an insulator as the R^{3+} ionic radius decreases (Fig. 1.2 (c))[1,6]. Moreover, a thermal metal-insulator transition occurs as a function of temperature in almost all compounds in this series, except *R* = Pr, which has the largest ionic radius among *R* (Fig. 1.2 (d))[6,7]. Subsequently, angle-resolved photoemission spectroscopy (ARPES) revealed that this paramagnetic metal $Pr_2Ir_2O_7$ has a quadratic-band touching state across the Fermi level[8], whereas the ARPES measurement showed that $Nd_2Ir_2O_7$ has a quadratic-band touching above its Néel temperature and a Mott gap state at low temperature[9].

This quadratic band touching state can evolve into abundant topological phases by symmetry-breaking perturbation[8,10]. For example, (Nd, Pr)$_2$Ir$_2$O$_7$ solid solution has been reported to exhibit anomalous Hall conductance, which may be attributable to its WSM state under various external perturbations, such as high pressure and a magnetic field[11–13]. Moreover, charge dynamics arising from the optical conductivity of Nd$_2$(Ir$_{1-x}$Rh$_x$)$_2$O$_7$ with different Rh-ion contents suggested that the ground-state phase differs among narrow-gap Mott insulators, WSMs, and correlated metals[14,15]. Importantly, these observations were limited to bulk solid solutions where the dopant-induced disorder can affect their physical properties[16,17]. In addition, these observations were made under high pressure and a magnetic field which makes ARPES measurement not applicable. Therefore, the clear observation and control of such topological phases have remained elusive.

The main limitation in experimental studies of bulk $R_2Ir_2O_7$ is that topological states are hidden by cubic crystalline symmetry. For example, the predicted WSM state in $R_2Ir_2O_7$ bulk theoretically has pairs of the Weyl nodes in the Brillion zone[18,19]. The summation of each pair of the Weyl nodes can lead to an intrinsic anomalous Hall effect accompanied by the magnetic order, which can be direct evidence of the magnetic WSM state in $R_2Ir_2O_7$ bulk. However, cubic symmetry of bulk $R_2Ir_2O_7$ induces a complete cancellation of the Chern vectors resulting in a zero net anomalous Hall conductance[20]. Breaking the cubic symmetry should lead to incomplete cancellation of the Chern vectors for unveiling a nonzero anomalous Hall conductance[20]. Such breaking of cubic symmetry can be experimentally realized by either applying a biaxial (or uniaxial) strain[20,21] or by confining the pyrochlore lattice into a slab geometry, along the [111] crystalline direction[20,22]. In this sense, the thin film offers a suitable platform for additional control over the crystalline symmetry and lattice deformation by

leveraging epitaxial mismatch strain.

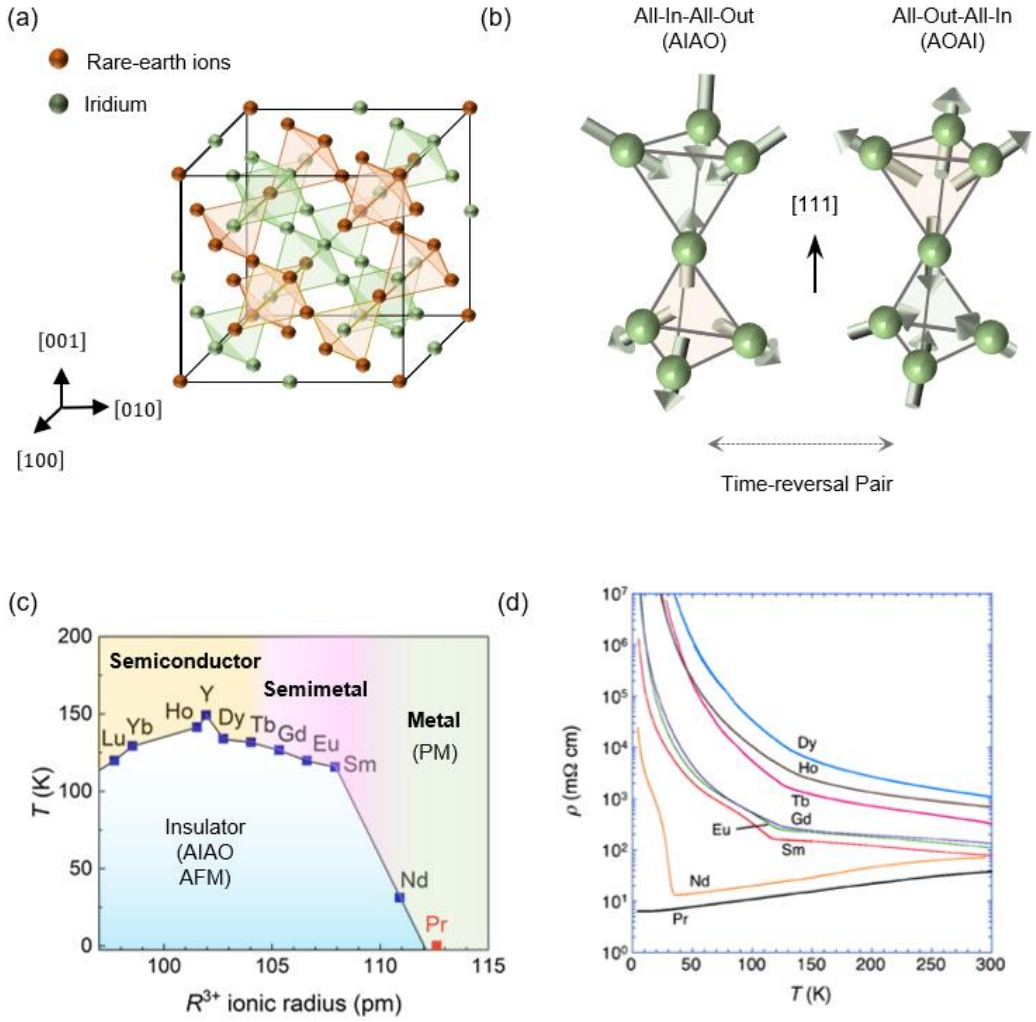

Figure 1.4 a) Schematic of the $R_2Ir_2O_7$ structure and (b) all-in-all-out (all-out-all-in) spin ordering. (c) Phase diagram for $R_2Ir_2O_7$ based on transport and magnetism measurements, modified based on the diagrams in Ref. [13]. (d) Electrical resistivities of $R_2Ir_2O_7$ bulk[6].

1.3 Why thin film?

The research in pyrochlore iridate limited the research to the bulk system. In bulk $R_2Ir_2O_7$, the electronic ground states change from a metal to an insulator as the R^{3+} ionic radius decreases. In addition, the MIT occurs as a function of temperature in almost all members of the family except $Pr_2Ir_2O_7$, which has the largest ionic radius. Later, the angle-resolved photoemission spectroscopy (ARPES) revealed the quadratic band touching state across the Fermi level in $Pr_2Ir_2O_7$. This quadratic band touching state can be evolved into CTPs by symmetry-breaking perturbation such as chemical doping and high pressure and magnetic field. Importantly, these perturbation methods can critically affect the ARPES measurement with the disorder. Lastly, the pyrochlore iridate has Fd3m cubic crystalline symmetry. Such symmetry leads to a net zero of Berry curvature induced by Weyl points. As a consequence, the Berry curvature-induced anomalous Hall effect (AHE) vanishes.

Pyrochlore thin films allow tuning of ground states and associated physical properties in terms of the epitaxial strain. Having similar orders of magnitude of Coulomb interaction (U) and spin-orbit coupling (λ), 5*d* electron systems, such as iridates, are well suited for identifying novel topological phases. Many theoretical studies have shown that numerous topological phases can be observed by tuning U/t (t: hopping parameter) and λ/t in solid material systems (Fig. 1.2(a))[6,23]. Notably, the biaxial tensile (compressive) strain on $R_2Ir_2O_7$ thin film can tune the Ir-O-Ir bonding angle closer to (further from) 180°, which increases (decreases) the magnitude of t (Ref. [1]). This strain tunability of t (or U/t and λ/t) is shown in the phase diagram in Fig. 1.1.

The epitaxial strain on pyrochlore iridate films can also break the cubic symmetry of the AIAO order, thus generating emergent phenomena that are hidden in the bulk phase[20–22]. For

example, applying compressive biaxial strain to (111)-oriented $R_2Ir_2O_7$ will break the cubic symmetry of AIAO spin orders (Fig. 1.2(b)). This strained AIAO has three irreducible representation bases, i.e., dipole, A_2-octupole, and T_1-octupole, while regular AIAO has only the A_2-octupole[24]. From the viewpoint of cluster multipole theory, the T_1-octupole has a symmetry that allows spontaneous Hall conductivity, which is forbidden for regular AIAO ordering[24,25]. As the magnetism is often coupled to the electronic ground state, this tunability of spin order symmetry provides an opportunity to explore exotic correlated ground states.

Another advantage of pyrochlore films is that their dimensionality can be controlled by thinning. In particular, *en route* to the two-dimensional limit from the three-dimensional limit, the hidden topological states may appear in the electron band structure[20,22]. Specifically, a quantum confinement effect is expected when the film thickness that are on the scale of the electron wavelength. Then, the quantum anomalous Hall effect (AHE) can emerge from its gapless surface states in a few unit cells of $R_2Ir_2O_7$ (Ref. [20,22]). In addition, with the formation of a heterostructure and by combining the pyrochlore iridate layer with other material, we can expect intriguing phenomena at their interface. A couple of theoretical studies predicted that topologically non-trivial states could emerge at the interface between $R_2Ir_2O_7$ and a nonmagnetic bandgap insulator[26,27]. As a promising means of exploring intriguing phenomena in $R_2Ir_2O_7$, thin films provide control over crystalline symmetry, dimension, and lattice deformation by imposing strain (Fig. 1.3).

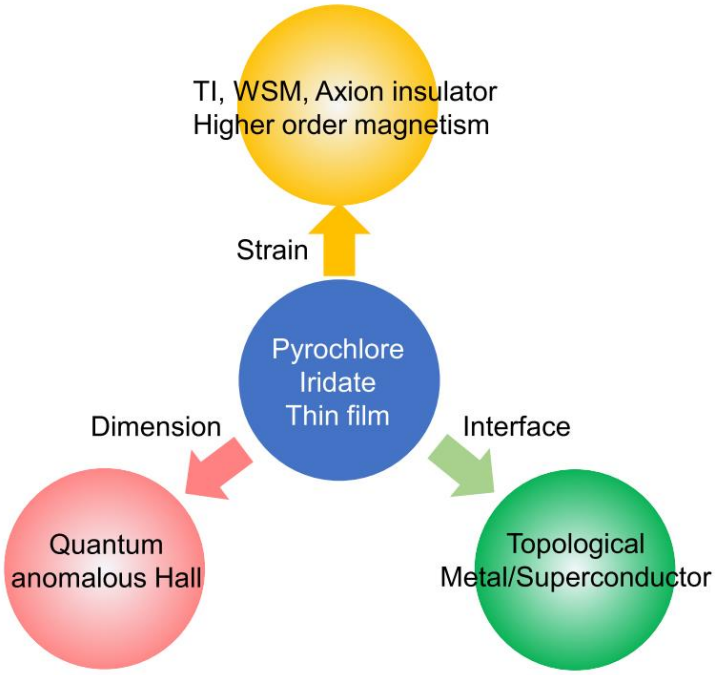

Figure 1.3 Schematic diagram showing advantage of pyrochlore iridate thin film. Adapt from[28]

1.2 Outline of the thesis

In this thesis, I will discuss about the anomalous magnetotransport in fully-strained $Nd_2Ir_2O_7$ (NIO-227) thin films. I start with the study on the growth mechanism of NIO-227 film, which is specially designed to obtain the high-quality pyrochlore iridate thin film. Next, I will discuss anomalous magnetotransport such as AHE and planar Hall effect in fully-strained NIO-227 film. Particularly, the anomalous magnetotransport in NIO-227 film is related to strain-induced antiferromagnetic spin texture called cluster magnetic octupole.

References

1. Witczak-Krempa, W., Chen, G., Kim, Y. B. & Balents, L. Correlated Quantum Phenomena in the Strong Spin-Orbit Regime. *Annu. Rev. Condens. Matter Physics, Vol 5* **5**, 57–82 (2014).
2. Wan, X., Turner, A. M., Vishwanath, A. & Savrasov, S. Y. Topological semimetal and Fermi-arc surface states in the electronic structure of pyrochlore iridates. *Phys. Rev. B* **83**, 205101 (2011).
3. Yang, B.-J. & Kim, Y. B. Topological insulators and metal-insulator transition in the pyrochlore iridates. *Phys. Rev. B* **82**, 85111 (2010).
4. Varnava, N. & Vanderbilt, D. Surfaces of axion insulators. *Phys. Rev. B* **98**, 245117 (2018).
5. Oh, T., Ishizuka, H. & Yang, B.-J. Magnetic field induced topological semimetals near the quantum critical point of pyrochlore iridates. *Phys. Rev. B* **98**, 144409 (2018).
6. Matsuhira, K., Wakeshima, M., Hinatsu, Y. & Takagi, S. Metal–Insulator Transitions in Pyrochlore Oxides $Ln_2Ir_2O_7$. *J. Phys. Soc. Japan* **80**, 94701 (2011).
7. Nakatsuji, S. *et al.* Metallic Spin-Liquid Behavior of the Geometrically Frustrated Kondo Lattice $Pr_2Ir_2O_7$. *Phys. Rev. Lett.* **96**, 87204 (2006).
8. Kondo, T. *et al.* Quadratic Fermi node in a 3D strongly correlated semimetal. *Nat. Commun.* **6**, 10042 (2015).
9. Nakayama, M. *et al.* Slater to Mott Crossover in the Metal to Insulator Transition of $Nd_2Ir_2O_7$. *Phys. Rev. Lett.* **117**, 56403 (2016).
10. Moon, E.-G., Xu, C., Kim, Y. B. & Balents, L. Non-Fermi-Liquid and Topological States with Strong Spin-Orbit Coupling. *Phys. Rev. Lett.* **111**, 206401 (2013).
11. Ueda, K. *et al.* Spontaneous Hall effect in the Weyl semimetal candidate of all-in all-

out pyrochlore iridate. *Nat. Commun.* **9**, 3032 (2018).

12. Ueda, K. *et al.* Magnetic Field-Induced Insulator-Semimetal Transition in a Pyrochlore $Nd_2Ir_2O_7$. *Phys. Rev. Lett.* **115**, 56402 (2015).
13. Ueda, K. *et al.* Magnetic-field induced multiple topological phases in pyrochlore iridates with Mott criticality. *Nat. Commun.* **8**, 15515 (2017).
14. Ueda, K. *et al.* Variation of Charge Dynamics in the Course of Metal-Insulator Transition for Pyrochlore-Type $Nd_2Ir_2O_7$. *Phys. Rev. Lett.* **109**, 136402 (2012).
15. Ueda, K. *et al.* Anomalous domain-wall conductance in pyrochlore-type $Nd_2Ir_2O_7$ on the verge of the metal-insulator transition. *Phys. Rev. B* **89**, 75127 (2014).
16. Lee-Hone, N. R., Dodge, J. S. & Broun, D. M. Disorder and superfluid density in overdoped cuprate superconductors. *Phys. Rev. B* **96**, 24501 (2017).
17. Lee-Hone, N. R., Mishra, V., Broun, D. M. & Hirschfeld, P. J. Optical conductivity of overdoped cuprate superconductors: Application to $La_{2-x}Sr_xCuO_4$. *Phys. Rev. B* **98**, 54506 (2018).
18. Armitage, N. P., Mele, E. J. & Vishwanath, A. Weyl and Dirac semimetals in three-dimensional solids. *Rev. Mod. Phys.* **90**, 15001 (2018).
19. Burkov, A. A. Weyl Metals. *Annu. Rev. Condens. Matter Phys.* **9**, 359–378 (2018).
20. Yang, B.-J. & Nagaosa, N. Emergent Topological Phenomena in Thin Films of Pyrochlore Iridates. *Phys. Rev. Lett.* **112**, 246402 (2014).
21. Yang, K.-Y., Lu, Y.-M. & Ran, Y. Quantum Hall effects in a Weyl semimetal: Possible application in pyrochlore iridates. *Phys. Rev. B* **84**, 75129 (2011).
22. Hwang, K. & Kim, Y. B. Theory of Multifarious Quantum Phases and Large Anomalous Hall Effect in Pyrochlore Iridate Thin Films. *Sci. Rep.* **6**, 30017 (2016).
23. Morimoto, T. & Nagaosa, N. Weyl Mott Insulator. *Sci. Rep.* **6**, 19853 (2016).

24. Suzuki, M.-T., Koretsune, T., Ochi, M. & Arita, R. Cluster multipole theory for anomalous Hall effect in antiferromagnets. *Phys. Rev. B* **95**, 94406 (2017).
25. Jin, K. W. *et al.* Strain engineering of the magnetic multipole moments and anomalous Hall effect in pyrochlore iridate thin films. *Sci. Adv.* **6**, eabb1539 (2022).
26. Laurell, P. & Fiete, G. A. Topological Magnon Bands and Unconventional Superconductivity in Pyrochlore Iridate Thin Films. *Phys. Rev. Lett.* **118**, 177201 (2017).
27. Hu, X., Zhong, Z. & Fiete, G. A. First Principles Prediction of Topological Phases in Thin Films of Pyrochlore Iridates. *Sci. Rep.* **5**, 11072 (2015).
28. Kim, W. J., Song, J., et al., Perspective on solid-phase epitaxy as a method for searching novel topological phases in pyrochlore iridate thin films. *APL Mater* **10**, 080901 (2022).

Chapter 2
Experimental Methods

2.1 Development of new growth methods via Pulsed Laser Deposition

Despite the extensive interest, the fabrication of high-quality single-crystalline (111) $R_2Ir_2O_7$ thin films remains challenging due to the formation of highly volatile gaseous iridium oxides (IrO_3) during growth[1]. The vapor pressure of IrO_3 is higher than that of other iridium oxides, such as IrO_2 and IrO. Such characteristics of IrO_3 result in substantial Ir loss during the growth under conditions where pyrochlore oxide form[2-4] (high pressure and temperature) (Fig. 2.1). Moreover, the IrO_2 can dissociate into Ir and O_2 in the pyrochlore oxide growth region[5-6]. This results in the formation of Ir metal. Because of these thermodynamic reactions, the growing pyrochlore iridate thin films by conventional methods such as molecular beam epitaxy and pulsed laser deposition were notoriously known to be difficult.

Part of Chapter 2 is published on APL Mater **10**, 080901 (2022)

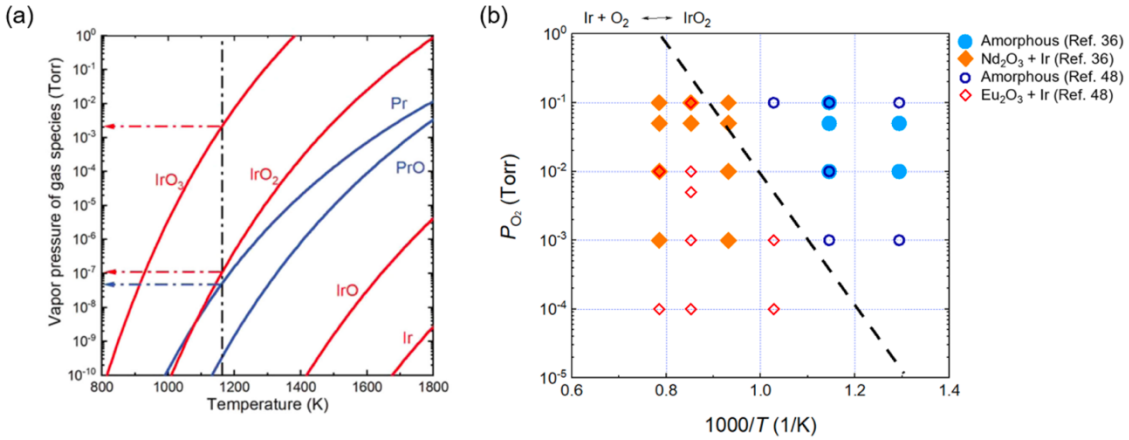

Figure 2.1 (a) Partial pressures of gas species in the IrO_2 and PrO_2 binary systems. [Reproduced with permission from Guo et al., npj Comput. Mater. **7**, 144 (2021).] (b) IrO_2 chemical reaction phase diagram. The dashed black line indicates the phase equilibrium line for Ir/IrO_2. On the left-side of the equilibrium line, Ir dissociation tends to occur, which leads to the Ir-deficient phase of the $R_2Ir_2O_7$ thin film. On the other hand, IrO_2 formation is preferable for the right-side of the equilibrium line. However, the temperature is not sufficiently high for crystalline $R_2Ir_2O_7$ thin film formation. Adapt from[2]

2.1.1 Solid phase epitaxy

To circumvent the thermodynamic reactions of IrO_2, the modified growth method is used to synthesize high-quality pyrochlore iridate thin films. Up until now, the most common way to synthesize pyrochlore iridate is the solid phase epitaxy (SPE) method[7-14]. The SPE method occurs when a metastable amorphous material is in close contact with a crystalline substrate. When heated, atoms in the amorphous phase reorder via local bond rearrangements at the interface between crystalline-amorphous interface. This process occurs entirely in the solid state; the resultant structure mimics the underlying crystalline substrate, which acts as a template. This method has been used for many types of materials, including Si-based semiconducting materials. One particular case of SPE has been of practical interest for almost 60 years, i.e., the recrystallization of Si crystals after doping by ion implantation; the results for this process are optimal when the surface of the Si crystal is first amorphized by Si ion implantation. SPE converts the silicon back to the crystalline state while keeping the implanted dopants within the Si film, where they can be electrically active. A similar type of growth was also applied to GaAs where a deposited amorphous film crystallized upon annealing at low-temperature.

The underlying mechanism of SPE can be understood by a thermodynamic relation. When amorphous solids crystallize, the Gibbs free energy is reduced. Then, the net free energy change after amorphous solid crystallization is

$$\Delta G = \frac{S\Delta x\rho}{W(G_c - G_A)},$$

Where G_c and G_A are the Gibbs energies per mole of the crystalline and amorphous phases, respectively; Δx is the crystallized thickness; S is the area; ρ is the density (g/volume); and W is the molar weight (g mol^{-1}). When $G_A > G_c$, ΔG is negative, and therefore, the transition from

amorphous solid to crystallized solid is possible.

If thermodynamic conditions are suitable for the crystallization of the amorphous solid, the SPE is useful for the synthesis of volatile compounds into epitaxial thin film[15]. Since the amorphous layer is grown at relatively low temperatures this can suppress the volatile compound to evaporate during the growth. Considering the volatile nature of Ir under conditions of high pressure and high temperature, SPE provides a great opportunity for $R_2Ir_2O_7$ thin film growth.

In 2015 Fujita *et al*. demonstrated that SPE can be used to synthesize $Eu_2Ir_2O_7$ thin films[7-8]. To synthesize $Eu_2Ir_2O_7$ thin films, they used conventional two-step SPE, as shown schematically in Fig. 2.2 (a). In this method, the amorphous $Eu_2Ir_2O_7$ film is first deposited on yttria-stabilized zirconia (YSZ). Because its lattice parameters are like those of $R_2Ir_2O_7$ (e.g., a = 10.27 Å for R = Eu)[9], the cubic YSZ substrate (2a = 10.24 Å) provides a suitable template for SPE growth. Then, ex-situ post-annealing of this amorphous film is performed in a sealed tube (Fig 2.2). This method solves the problem of IrO_3 volatility by first depositing the amorphous phase under conditions suitable for a stoichiometric balance of elements, followed by post-annealing at high temperatures in the air to induce crystallization. Note that some studies added IrO_2 powders and performed post-annealing in combination with the amorphous $R_2Ir_2O_7$ film to avoid Ir loss. Scanning transmission electron microscopy (STEM) image of SPE-grown $Eu_2Ir_2O_7$/YSZ (111) in Fig. 2.2 (b) shows an epitaxial relationship between the film and substrate. This method has been extended to various $R_2Ir_2O_7$ syntheses by many other groups.

As we discussed in the introduction section of this paper, the observation of an intrinsic anomalous Hall effect from non-zero Chern vectors would be one of the evidence for the magnetic topological phases in pyrochlore iridates[10,11]. Although electrical transport can probe

such non-trivial topological properties, the more direct way to observe the topological band structure in the momentum space of the material would be the ARPES measurement. For example, ARPES measurements have revealed the 3D linearly dispersive bulk Weyl cones and Weyl nodes in TaAs[12,13]. Their measurement demonstrated the existence of the Fermi arc surface states connecting the projection of bulk Weyl nodes in the surface Brillouin zone. These studies indicate that ARPES is a powerful tool for investigating the surface and bulk electronic structure of topological materials. However, the ARPES measurement on pyrochlore thin film is difficult due to the sample quality issues, which will be discussed in more detail in the next section. Therefore, most reported studies of pyrochlore iridate thin film studies are confined to the transport measurements which will be discussed in this section.

By allowing the successful synthesis of $R_2Ir_2O_7$ thin films, SPE provides an opportunity to study electronic transport properties in thin films that do not often appear in bulk crystal form. Particularly, the well-defined crystalline structure with a large surface area of thin films allow analyses of their non-collinear magnetic ground state and associated magnetotransport behavior. For example, $Eu_2Ir_2O_7$/YSZ (111) thin film with an Ir-AIAO octupole moment[14] showed odd parity (or asymmetric) magnetoresistance (MR) behavior. This observation was intriguing because MR usually does not include an asymmetric term. Such unusual asymmetric MR can be explained by the canting effect on non-collinear AIAO under the external magnetic field[7].

Moreover, unusual AIAO/AOAI domain wall conduction has been extensively studied in $R_2Ir_2O_7$/YSZ (111) films. Large electrical conductance at the domain wall, which may have been related to its proximity to the metal-insulator transition, has been observed in bulk $R_2Ir_2O_7$ crystals[15]. However, thin film geometry can enhance the contribution of the magnetic domain wall response[16]. For example, creating a large AIAO/AOAI domain wall at the heterointerface

in $Eu_2Ir_2O_7/Tb_2Ir_2O_7$/YSZ (111) made it possible to measure domain wall sheet conductance[17]. In addition, large anomalous Hall conductance was observed in $Nd_2Ir_2O_7$/YSZ (111) thin film, where the magnetic field was applied around the coercive field for domain switching[18]. This implies that the formation of a domain wall from a given crystal symmetry naturally breaks the cubic symmetry and is responsible for the observed large AHE.

In addition to the AHE that arises from domain switching, the spontaneous Hall effect (i.e., without magnetization) has recently been reported in $Pr_2Ir_2O_7$ thin film. In bulk $Pr_2Ir_2O_7$, the spontaneous Hall effect due to spin chirality from Pr 4*f* moments was previously reported to be below 1.5 K (Ref. [19]). Surprisingly, in $Pr_2Ir_2O_7$ thin film, a spontaneous Hall effect started to appear near 50 K (Ref. [20,21]). Ohtsuki *et al*. have suggested that slight strain can induce a WSM state by breaking the cubic symmetry within AIAO magnetic order and responsible for observed spontaneous Hall effect[21]. This argument was later expanded by Li *et al*., who showed that the twofold oscillation in the planar Hall effect is due to a chiral anomaly, while additional oscillation is due to AIAO ordering in $Pr_2Ir_2O_7$ thin film[20]. However, no magnetic signals associated with long-range order were revealed by resonant scattering measurements in $Pr_2Ir_2O_7$ thin film. Guo *et al*. argued that the spontaneous Hall effect is due to the spin chirality arising from localized Ir-moments ordering[22].

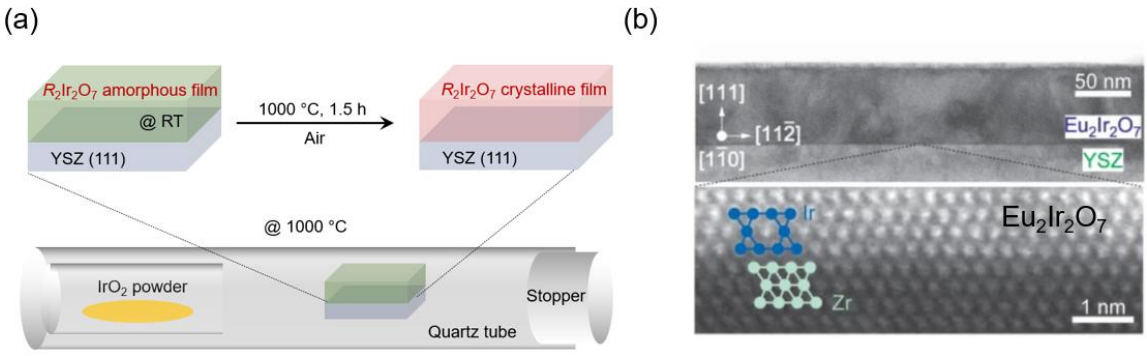

Figure 2.2 (a) Schematic of the conventional SPE method. (b) Phase-contrast image of high-resolution TEM of a $Eu_2Ir_2O_7$ (111) film on a YSZ (111) substrate. [Rep. **5**, 9711 (2015)]

2.1.2 Repeated Rapid High-T Synthesis Epitaxy

Although SPE allows the synthesis and investigation of pyrochlore iridate thin films, this method has a few critical limitations in investigating the CTPs. Because the SPE method involves *ex-situ* thermal annealing, the resulting film has mediocre surface roughness and poor interface. This resulted in restraint on electronic structure measurement such as ARPES and scanning tunneling microscopy, which requires atomically flat surfaces. Furthermore, most SPE-grown pyrochlore iridate thin films have bulk-like crystalline structures (relaxed film). As a result, the strain-induced CTPs cannot be investigated.

Thus far, the application of epitaxial strain to pyrochlore iridate thin film has been achieved with repeated rapid high-T synthesis epitaxy (RRHSE) method[23-25]. The RRHSE process involves two key steps in a thermal cycle using pulsed laser deposition (PLD) (Fig. 2.3). The commercial PLD from Pascal was used. The temperature (T) is maintained at medium (~ 600 ºC), while oxygen pressure (PO_2) is kept fixed at 50 mTorr. After stabilizing the T and PO_2, the pyrochlore iridate polycrystalline target is ablated. To compensate for any Ir-loss that may occur during the process, the additional IrO_2 target (Toshima Manufacturing Co. Ltd) is ablated. In the second step, the pyrochlore phase is formed through rapid thermal annealing. The sample is rapidly heated to 850 ºC at a rate of 400 ºC/min using a diode laser heater. Then, the sample is maintained at 850 ºC for a short period to synthesize the pyrochlore phase while minimizing Ir loss.

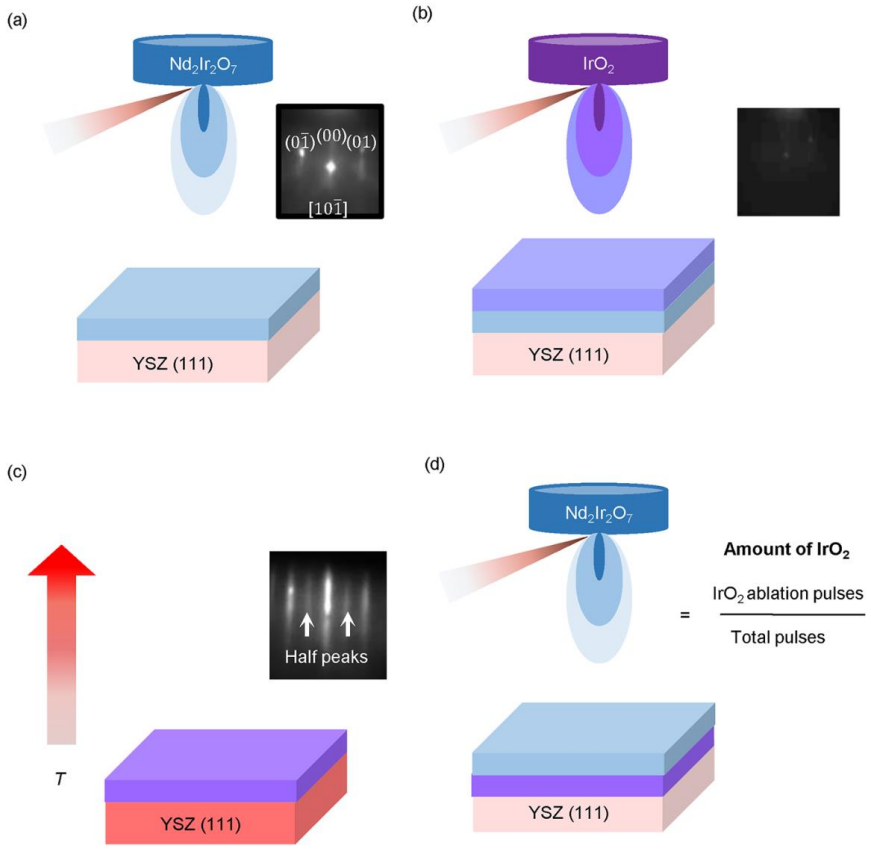

Figure 2.3 Growth of strained Nd2Ir2O7 (NIO-227) thin films via repeated rapid high-temperature synthesis epitaxy (RRHSE). NIO-227 films were deposited on [111] oriented yttria-stabilized zirconia (YSZ) substrates using the RRHSE method. (a)–(d) illustrate each step of the RRHSE method, respectively. (a) The first step of the RRHSE process is the ablation of the polycrystalline NIO-227 target on YSZ (111) at 600°C. (b) The second step of the RRHSE method is the ablation of the IrO2 target. The additional ablation of the IrO2 target compensates for the severe Ir loss during the deposition of NIO-227 film. (c) The third step of the RRHSE method is the rapid thermal annealing of the sam- ple from steps (a) and (b) at high T to form the pyrochlore phase, with a rapid temperature increase of 400°C/min to 850°C. (d) After annealing the sample, the steps in (a)–(c) are repeated to achieve the desired thickness of films. Adapt from[23].

2.2 Sample structural characterization

X-ray diffraction (XRD, D8 Discover; Bruker) with a Cu Kα-1 source (l = 1.5406 Å) were used to characterize the crystallinity of films grown by the RRHSE method. The lattice parameters, crystallinity, and film thickness were determined by using Bragg's law. Furthermore, the reciprocal space mapping (RSM) technique is used to determine the existence of epitaxial strain. Also, atomic forced microscopy (AFM, Cypher; Asylum Research) was used to characterize the surface topography of thin films and substrates.

2.3 Magnetotransport measurements

The electrical resistivity of thin films and magnetotransport of pyrochlore iridate thin films were measured using a four-probe method using physical property measurement system (Quantum Design Inc.). While the electrical resistivity of thin films with temperature variation is widely used to probe the physical properties of the sample, magnetotransport measurements such as AHE and planar Hall effect (PHE) are used to probe the magnetic properties of the sample.

For magnetotransport and temperature-dependent resistivity, a Hall bar device on the thin films was fabricated. To avoid the contact resistance effect, the Hall bar was designed for four-probe geometry. 50 nm of Au electro-rode was deposited with electron beam evaporation. Moreover, the magnetic properties of the film were measured by magnetic properties measurement system (MPMS, Quantum Design). We polished the back side of the samples to remove the possible magnetic signal from the substrate and Pt paste used during the growth.

References

1. Chakhalian, J., Liu, X. & Fiete, G. A. Strongly correlated and topological states in [111] grown transition metal oxide thin films and heterostructures. *APL Mater.* **8**, 50904 (2020).
2. Kim, W. J., Song, J., et al., Perspective on solid-phase epitaxy as a method for searching novel topological phases in pyrochlore iridate thin films. *APL Mater* **10**, 080901 (2022).
3. Guo, L. *et al.* Searching for a route to synthesize in situ epitaxial $Pr_2Ir_2O_7$ thin films with thermodynamic methods. *npj Comput. Mater.* **7**, 144 (2021).
4. M. Asadian, in *Modern Aspects of Bulk Crystal and Thin Film Preparation*, edited by Nikolai Kolesnikov and Elena Borisenko (IntechOpen, 2012).
5. Yang, W. C. *et al.* Epitaxial thin films of pyrochlore iridate $Bi_{2+x}Ir_{2-y}O_{7-\delta}$: structure, defects and transport properties. *Sci. Rep.* **7**, 7740 (2017).
6. Gallagher, J. C. *et al.* Epitaxial growth of iridate pyrochlore $Nd_2Ir_2O_7$ films. *Sci. Rep.* **6**, 22282 (2016).
7. Fujita, T. C. *et al.* Odd-parity magnetoresistance in pyrochlore iridate thin films with broken time-reversal symmetry. *Sci. Rep.* **5**, 9711 (2015).
8. Fujita, T. C. *et al.* All-in-all-out magnetic domain size in pyrochlore iridate thin films as probed by local magnetotransport. *Appl. Phys. Lett.* **108**, 22402 (2016).
9. Shapiro, M. C. *et al.* Structure and magnetic properties of the pyrochlore iridate $Y_2Ir_2O_7$. *Phys. Rev. B* **85**, 214434 (2012).
10. Armitage, N. P., Mele, E. J. & Vishwanath, A. Weyl and Dirac semimetals in three-dimensional solids. *Rev. Mod. Phys.* **90**, 15001 (2018).
11. Burkov, A. A. Weyl Metals. *Annu. Rev. Condens. Matter Phys.* **9**, 359–378 (2018).
12. Xu, S.-Y. *et al.* Discovery of a Weyl fermion semimetal and topological Fermi arcs.

Science (80-.). **349**, 613–617 (2015).

13. Lv, B. Q. *et al.* Experimental Discovery of Weyl Semimetal TaAs. *Phys. Rev. X* **5**, 31013 (2015).
14. Arima, T. Time-Reversal Symmetry Breaking and Consequent Physical Responses Induced by All-In-All-Out Type Magnetic Order on the Pyrochlore Lattice. *J. Phys. Soc. Japan* **82**, 13705 (2012).
15. Ma, E. Y. *et al.* Mobile metallic domain walls in an all-in-all-out magnetic insulator. *Science (80-.).* **350**, 538 (2015).
16. Fisher, M. E. & Ferdinand, A. E. Interfacial, Boundary, and Size Effects at Critical Points. *Phys. Rev. Lett.* **19**, 169–172 (1967).
17. T. C. Fujita *et al.*, Phys. Rev. B **93**, 064419 (2016).
18. W. J. Kim *et al.*, Phys. Rev. B **98**, 125103 (2018).
19. Machida, Y., Nakatsuji, S., Onoda, S., Tayama, T. & Sakakibara, T. Time-reversal symmetry breaking and spontaneous Hall effect without magnetic dipole order. *Nature* **463**, 210 (2009).
20. Li, Y. *et al.* Correlated Magnetic Weyl Semimetal State in Strained $Pr_2Ir_2O_7$. *Adv. Mater.* **33**, 2008528 (2021).
21. Takumi, O. *et al.* Strain-induced spontaneous Hall effect in an epitaxial thin film of a Luttinger semimetal. *Proc. Natl. Acad. Sci.* **116**, 8803–8808 (2019).
22. Guo, L. *et al.* Spontaneous Hall effect enhanced by local Ir moments in epitaxial $Pr_2Ir_2O_7$ thin films. *Phys. Rev. B* **101**, 104405 (2020).
23. J. Song *et al*., Engineering structural homogeneity and magnetotransport in strained $Nd_2Ir_2O_7$ films. APL Mater. **11**, 061104 (2023).
24. J. Song *et al*., Higher harmonics in planar Hall effect induced by cluster magnetic multipoles. *Nat Commun* **13**, 6501 (2022).

25. Jin, K. W. *et al.* Strain engineering of the magnetic multipole moments and anomalous Hall effect in pyrochlore iridate thin films. *Sci. Adv.* **6**, eabb1539 (2022).

Chapter 3

Engineering structure homogeneity and magnetotransport in strained $Nd_2Ir_2O_7$ thin films

3.1 Introduction

Searching for quantum materials with nontrivial band topology is currently one of the central themes in both materials science and condensed matter physics[1]. The family of 5*d* pyrochlore iridates ($R_2Ir_2O_7$, R = rare earth ions) has gained significant interest due to the interplay between comparable strength of the parameters such as the Coulomb interaction (U) and spin-orbit coupling (λ)[2-17]. This interplay is predicted to result in a fertile topological state of matter, including a topological insulator[6,17], Weyl semimetallic state[2-4,8], and axion insulator[5]. Moreover, bulk $R_2Ir_2O_7$ exhibits an all-in-all-out (AIAO) antiferromagnetic ordering configuration[3]. This AIAO ordering spontaneously breaks the time-reversal symmetry without reducing cubic crystalline symmetry. Such symmetry breaking by AIAO ordering is highly suitable for exotic phenomena arising from nontrivial topological states, such as large anomalous Hall effect (AHE) and quantized AHE[8].

$R_2Ir_2O_7$ thin films offer a suitable platform to investigate topological phases and exotic phenomena, which are hidden in bulk due to cubic crystalline symmetry[8,18-19]. The epitaxial strain can break cubic crystalline symmetry, resulting in nonvanishing AHE. Particularly, recent theoretical works[7-8, 20-23] have revealed the investigation of various topological phenomena in [111] oriented $R_2Ir_2O_7$ thin films through tuning U and λ. This is achieved by applying biaxial compressive or tensile strain along [111] direction, which adjusts the Ir-O-Ir bonding angle. Such tunability provides control over the electron hopping (t), U/t, and λ/t,

Part of Chapter 3 is published on APL Mater **11**, 061104 (2023)

allowing access to hidden topological phenomena such as chiral magnetic metal and unconventional superconductivity[7-8, 20-23].

Part of Chapter 3 is published on APL Mater **11**, 061104 (2023)

3.1.1 Impurities induced by characteristics of IrO_2

Despite the extensive interest, the fabrication of high-quality single-crystalline (111) $R_2Ir_2O_7$ thin films remains challenging due to the formation of highly volatile gaseous iridium oxides (IrO_3) during growth[24-26]. The formation of IrO_3 leads to the dramatic loss of Ir and the formation of secondary chemical phases and defects in the film. The vast majority of successfully grown $R_2Ir_2O_7$ thin films have been realized via the two-step protocol[27-40] called "solid phase epitaxy (SPE)." However, the SPE method produces either relaxed or partially-strained $R_2Ir_2O_7$ films, which is not ideal for investigating strain-induced topological phenomena. In this chapter, I will discuss the control of defects and impurities in (111) oriented strained pyrochlore $Nd_2Ir_2O_7$ (NIO-227) thin films by adjusting the amount of additional IrO_2 target ablation.

3.1.2 Compensating Ir loss during the growth

The RRHSE (repeated rapid high-temperature synthesis epitaxy) process for synthesizing NIO-227 films involves two key steps in a thermal cycle using pulsed laser deposition (PLD). The temperature (*T*) is maintained at 600 ºC, while the oxygen partial pressure (PO_2) is kept at 50 mTorr. The reflection high electron energy diffraction (RHEED) patterns near [101] peaks of the (111) oriented yttria-stabilized zirconia (YSZ) substrate are shown in Fig. 2.3a. After stabilizing the *T* and PO_2, we ablated the NIO-227 target to initiate the growth process (Fig. 2.3a). To compensate for any Ir-loss that may occur during the process, we then ablated the IrO_2 target (Fig. 2.3b). The decrease in RHEED patterns near [101] peaks during this first step indicates the formation of amorphous bilayers[41](Figs. 2.3a and 2.3b). Both targets were ablated by a KrF excimer laser (λ = 248 nm) and a frequency of 5Hz with a laser influence of 1.7 J/cm^2.

In the second step, the pyrochlore phase is formed through rapid thermal annealing. The sample is rapidly heated to 850 ºC at a rate of 400 ºC/min using a diode laser heater (Fig. 2.3c). Then, the sample is maintained at 850 ºC for a short period to synthesize the pyrochlore phase while minimizing Ir loss. Upon this thermal annealing step, we observed the appearance of additional half-order peaks in the RHEED pattern (Fig. 2.3c). Half-order peaks signify the formation of a new crystalline layer with unit-cell doubling relative to the YSZ substrate. After the thermal annealing process, the temperature of the sample is decreased to 600 ºC, and the two steps are repeated to attain the desired thickness of NIO-227 films, as illustrated in Fig. 2.1d. The RRHSE method differs from the conventional single target ablation PLD method in that it uses an additional ablation of the IrO_2 target to compensate for Ir loss. As a result, the amount of IrO_2 ablation should have an impact on the film structure.

3.2 Control of impurities during the growth via IrO_2 ablation

To understand the impact of the IrO_2 ablation on the NIO-227 film structure, we fabricated films on YSZ substrate with varying IrO_2 ablation. The percentage of IrO_2 ablation was calculated as $\frac{(IrO_2 \text{ ablation})}{(\text{total pulses})} \times 100$. Figure 3.1a shows the X-ray diffraction (XRD) pattern of films with IrO_2 ablation between 75 % - 95 %.). The XRD pattern of films with an amount of IrO_2 ablation not shown in Fig. 3.1a is shown in Fig. 3.2. When the IrO_2 ablation is below 70 %, the XRD pattern of the films displays peaks that do not correspond to NIO-227. However, by increasing the IrO_2 ablation to 75 % of the film, the XRD pattern shows satellite peaks near YSZ (111) and (222), indicating epitaxial growth of the film. These peaks do not correspond to NIO-227 (Fig. 3.1b) but may be attributed to Ir-deficient impurity phases such as Nd_3IrO_7, as reported in previous studies[25-26, 30]. Further increase of IrO_2 ablation from 75 % to 90 % leads to the appearance of "odd-numbered peaks" (111) and (333) in the XRD patterns of the films, indicating excellent crystallization of the pyrochlore phase[41-42]. The peaks in XRD patterns of the films with 85 % and 90 % IrO_2 ablation indicate the growth of high-quality NIO-227 films. Additionally, it is worth noting that the growth of strained NIO-227 films is sensitive to both the oxygen pressure and annealing temperature. Changes in these parameters during growth can result in the formation of impurities such as Ir metal or Ir-deficient Nd_2O_3 (as shown in Fig. 3.2). These impurities are induced by IrO_2 volatility or dissociation, highlighting the narrow growth window required for the successful production of strained NIO-227 films.

It is worth noting that the films produced with 80 % IrO_2 ablation display distinct characteristics compared to other NIO-227 films in terms of their XRD and reciprocal space mapping (RSM). As shown in Fig. 3.1b, the 80 % IrO_2 ablation film has peaks near odd-numbered peaks, but

they do not correspond to NIO-227. Furthermore, the RSM of both the 80 % and 90 % IrO_2 ablation films around YSZ (331) exhibit different features. As shown in Fig. 3.1c, both films have a peak around YSZ (331) in RSM. However, the peak of RSM in the 90 % IrO_2 ablation films has the same Q_x value as the YSZ (331) peak, indicating that the film is fully strained NIO-227. On the other hand, the peak of RSM in the 80 % IrO_2 ablation films has a lower intensity and is stretched longer along Q_z//[111]. This observation implies that the out-of-plane lattice is larger in the 80 % IrO_2 ablation film than in NIO-227 films. Additionally, the *c*-lattice constant of $d_{(444)}$ in the 80 % IrO_2 ablation film is larger than that of NIO-227 films (Fig. 3.1d). The correspondence *c*-lattice was derived from peaks in the XRD θ–2θ patterns using the Bragg's law equation, $n\lambda = 2d\sin(2\theta)$ ($\lambda = 1.5406$ Å). Based on the growth technique of RRHSE, the XRD and RSM features of the 80 % IrO_2 ablation films suggest the possible coexistence of Ir-deficient defects and a strained NIO-227 structure.

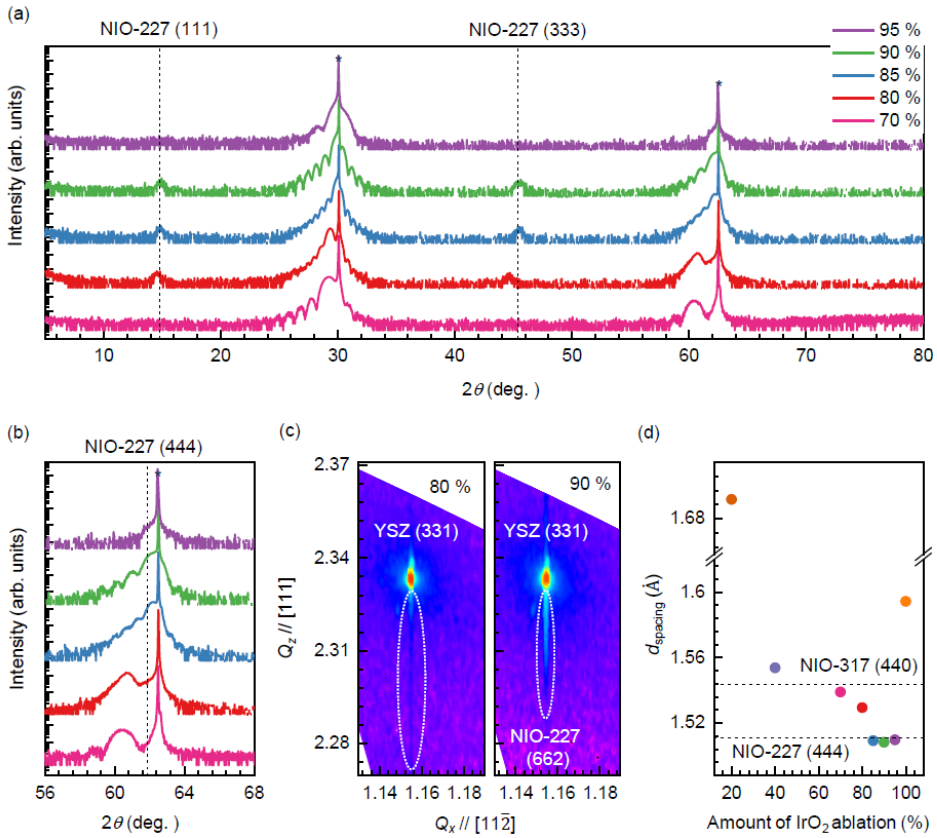

Figure 3.1 X-ray diffraction of NIO-227 films grown with different amounts of IrO_2 ablation (> 70 %). (a) X-ray diffraction (XRD) θ-2θ scans of NIO-227 films with different amounts of IrO_2 ablation ranging from 80 to 100 %. Films grown with 85 % IrO_2 ablation show strong NIO-227 signals, while films grown with 80 % IrO_2 ablation results in an off-stoichiometric sample. The asterisks (*) mark the YSZ substrate (111) and (222) peaks. YSZ Panel (b) provides a magnified view of the XRD patterns from (a), with the black dashed line indicating the position of the bulk NIO-227 (444) peak. (c) Reciprocal space map of the films grown with 80 % and 90 % IrO_2 ablation in the vicinity of the YSZ (331) reflection. The dashed lines present the peak position of the films. (d) By Bragg's law, the calculated *c* - lattice constant of all samples from the peaks near YSZ (222) is shown. The dashed line presents the position of the bulk NIO-227 (444).

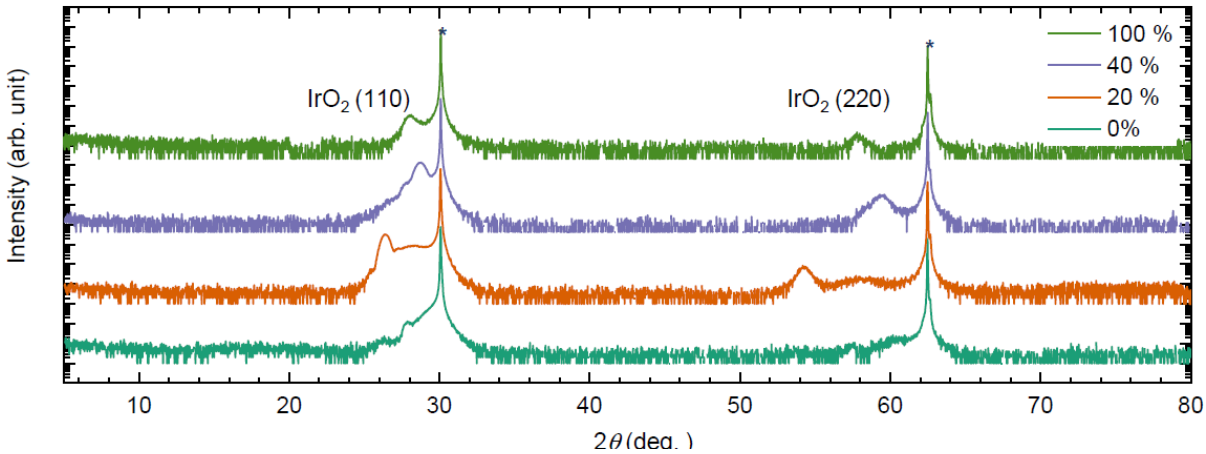

Figure 3.2 X-ray diffraction of NIO-227 films grown with different amounts of IrO_2 ablation.

X-ray diffraction (XRD) $\theta-2\theta$ scans of NIO-227 films with varying amounts of IrO_2 ablation (0 ~ 40 and 100 %).

Figure 3.3a and 3.3b display cross-sectional scanning transmission electron microscopy (STEM) images of films with 80 % and 90 % IrO_2 ablation, respectively. The 90 % IrO_2 ablation film displays a high-quality and homogeneous NIO-227 pyrochlore phase with a clear interface between YSZ and films. In contrast, the 80 % IrO_2 ablation film shows structural defects and an unclear interface in the NIO-227 region, as highlighted by the red lines. The STEM image of 80% IrO_2 ablation film indicates the coexistence of NIO-227 and defects, which can be attributed to Ir-loss during the growth. Furthermore, the STEM image of the 80% IrO_2 ablation film provides an explanation for the appearance of peaks near odd-numbered peaks, which are not characteristic of NIO-227 as being due to the presence of defects resulting from insufficient IrO_2 ablation.

The cross-sectional specimens for STEM measurement were prepared using focused ion beam milling (Helios G4; Thermo Fisher Scientific). Atomic-resolution HAADF STEM image in Figure 4a was acquired using a spherical aberration-corrected STEM (Themis Z; Thermo Fisher Scientific), operated at an electron acceleration voltage of 200 kV. The semi-convergence and inner semi-collection angles were set as 18.2 and 50 mrad, respectively. Atomic-resolution HAADF STEM image in Figure 4b was acquired using spherical aberration probe-corrected STEM (JEM-ARM 200F; JEOL Ltd., Tokyo, Japan) with an acceleration voltage of 80kV installed at the National Center for Inter-University Research Facilities (NCIRF), Seoul National University, South Korea. The semi-convergence and inner semi-collection angle for the imaging condition were employed to 24 and 80 mrad, respectively.

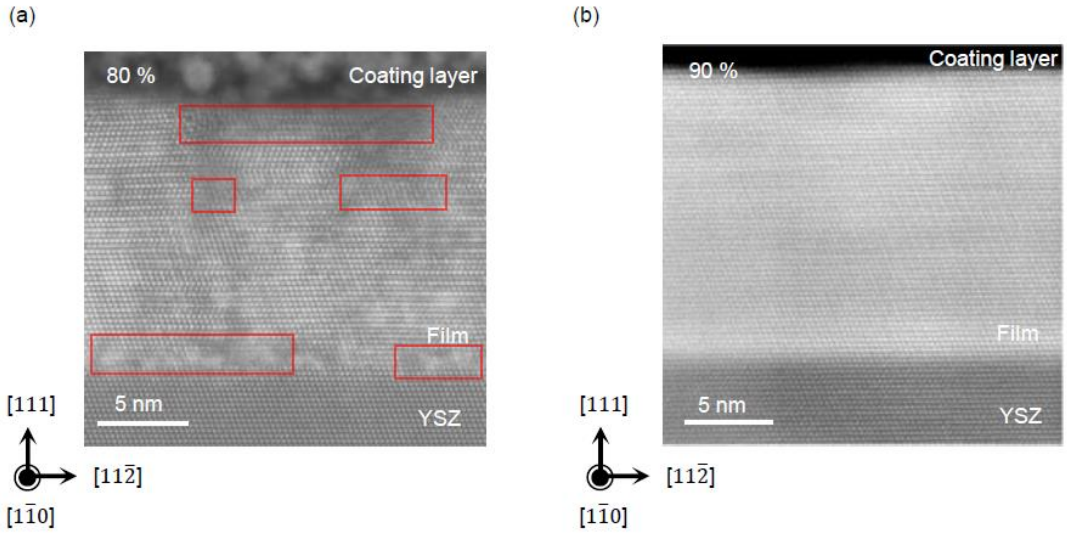

Figure 3.3 Cross-sectional scanning transmission electron microscopy images of films. High-angle annular dark field scanning transmission electron microscopy (HAADF-STEM) images of NIO-227 film grown with (a) 80 % IrO_2 ablation and (b) with 90 % IrO_2 ablation. The image of the NIO-227 film grown with 80 % IrO_2 ablation reveals inhomogeneity, with a cloudy region near the interface (highlighted in red). On the other hand, the image of the NIO-227 films grown with 90 % IrO_2 ablation shows homogeneity and high-quality.

3.3 Tuning metallicity and anomalous Hall effect

Next, we investigate the magnetotransport properties of the films. Figure 3.4a shows the longitudinal resistivity (ρ_{xx}) of the fabricated films above the 75 % IrO_2 ablation as a function of T, measured using Hall-bar geometry (inset of Fig. 3.4a) without an external magnetic field (H_{ext}). The magnetotransport properties of the NIO-227 films with IrO_2 ablation were studied using a standard four-point probe method with a commercial physical property measurement system (PPMS; Quantum Design Inc., San Diego, CA, USA). The electrical contacts were made by depositing a 50 nm-thick Au layer on the NIO-227 film using an e-beam evaporator. The current was applied along the $[1\bar{1}0]$ direction, while the magnetic field was applied in the [111] direction with a field sweep mode of $\pm$ 9 T for the anomalous Hall effect (AHE) measurement at 2 K. We observed two distinct features in ρ_{xx} for the 75 % and 80 % IrO_2 ablation films: an upturn in ρ_{xx} as T decreases and a decrease in ρ_{xx} at low T. The upturn of ρ_{xx} as T decreases in both films can be attributed to the presence of Ir-deficient impurity phases, which have been shown in previous studies[18,27,36] to cause an increase in ρ_{xx}, resulting in insulating behavior. Moreover, the ρ_{xx} at low T decreases by two orders of magnitude as the IrO_2 ablation increases from 75 % to 80 %. This change in ρ_{xx} can be attributed to a decrease in structural defects and a more homogeneous NIO-227 structure in the film, which were seen in the STEM image of 80 % IrO_2 ablation film (Fig. 3.3a). These results suggest that optimizing the IrO_2 ablation process can enhance the magnetotransport properties of NIO-227 films, which has important implications for their potential use in various electronic and spintronic applications.

The films exhibit semimetallic behaviors when the IrO_2 ablation reaches 85 %. As shown in Fig. 3.4a, the ρ_{xx} at low T decreases by two orders of magnitude as the IrO_2 increases

from 80 % to 85 %. This change in ρ_{xx} can be attributed to a further decrease in defects and structural inhomogeneity. Unlike bulk NIO-227, the NIO-227 films with 85%, 90 %, and 95 % IrO_2 ablation do not exhibit a metal-insulator transition (MIT). This distinct behavior of semimetallic NIO-227 films can be elucidated by the compressive strain effect[41-42]. According to the previous studies[41-42] of strained NIO-227 film, the valence and conduction bands move and cross near the Fermi level due to compressive strain. Notably, the ρ_{xx} reaches its lowest at 90 % IrO_2 ablation and slightly increases at 95 % IrO_2 ablation. The slight increase in ρ_{xx} can be associated with the disappearance of odd-numbered peaks and sample quality, indicating that 95 % IrO_2 ablation is excessive. Also, a recent experimental study on hydrothermally grown NIO-227 single crystals suggests that the transport properties can be enhanced by decreasing impurities in the crystal structure[43]. Therefore, the significant change in the resistivity of NIO-227 films can be attributed to a decrease in Ir-deficient impurities in NIO-227.

Furthermore, we measured the AHE (σ_{xy}^{AHE} ($H = \pm 9$ T)) of the films at 2 K, with a magnetic field (H_{ext}) applied along the [111] direction. As shown in Fig. 3.4b, the values of σ_{xy}^{AHE} (H) in the films increase as the structure of the films becomes more homogeneous NIO-227. The film with 75 % IrO_2 ablation exhibits almost zero σ_{xy}^{AHE} (H = - 9 T), while the film with 80 % IrO_2 ablation shows a finite value of σ_{xy}^{AHE} (H = - 9 T) ~ 0.45 Ω^{-1} cm^{-1}. In contrast, the film with 90 % IrO_2 ablation exhibits a maximum value of σ_{xy}^{AHE} (H = - 9 T) ~ 3.01 Ω^{-1} cm^{-1}. This increase in σ_{xy}^{AHE} in the films can be due to the improvement of the structure of the film, specifically, the enhancement of the (111) and (333) peaks.

The films also exhibit a hysteric feature of AHE with a finite value at 0 T, known as the spontaneous Hall effect (σ_{xy}^{AHE} (H = 0 T)). At 80 % IrO_2 ablation, the σ_{xy}^{AHE} (H = 0 T) is finite

(~ 0.09 Ω^{-1} cm^{-1}). The value of σ_{xy}^{AHE} (H = 0 T) reaches its maximum value (~ 1.51 Ω^{-1} cm^{-1}) at 90 % IrO_2 ablation (Fig. 3.4b) and decreases when IrO_2 ablation is further increased to 95 %. This emergence of σ_{xy}^{AHE} (H = 0 T) can be explained by the decrease in defects in NIO-227 films. The finite value of σ_{xy}^{AHE} (H = 0 T) in NIO-227 film is known as the strain-induced nontrivial contribution of antiferromagnetic ordering (T_1-octupole) to the Berry curvature[41-42]. The σ_{xy}^{AHE} should follow a $\propto \sigma_{xx}^{1.6}$ scaling relationship. Our films with NIO-227 structure (85%, 90 %, and 95 % IrO_2 ablation) fall on the $\sigma_{xy}^{AHE} \propto \sigma_{xx}^{1.6}$ relationship, whereas the films with defects (75 %and 80 % IrO_2 ablation) do not (Fig. 3.4c).

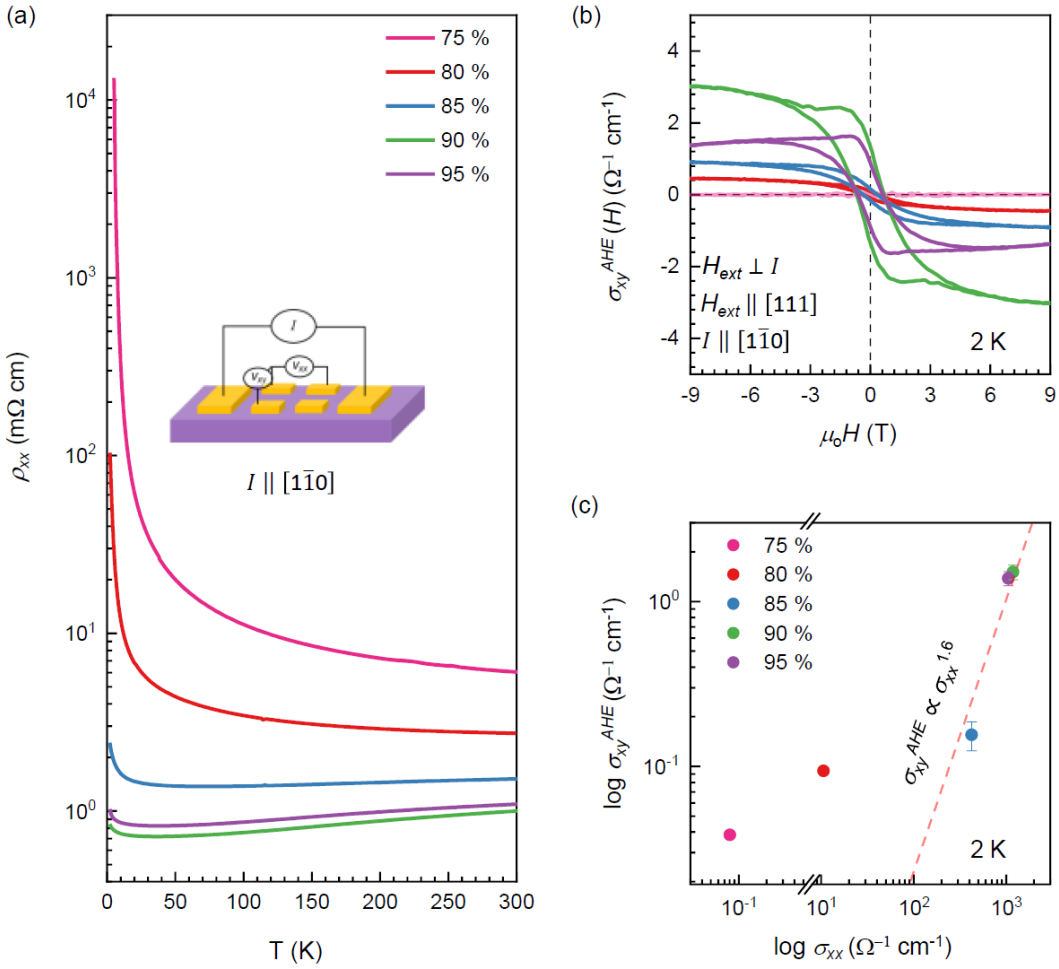

Figure 3.4 Intrinsic magnetotransport properties of the films with different amounts of IrO_2 ablation (> 70%) (a) The plot of the longitudinal resistivity, ρ_{xx}, vs. temperature, T, of NIO-227 films grown above 75 %. The schematic image shows the measurement direction where the current is applied [110] direction. (b) Anomalous Hall effects (AHE) measurement is performed with an external magnetic field (H_{ext}) applied along the [111] direction and current (I) flowing along the [110] direction at 2 K. (c) The log plot of σ_{xy}^{AHE} vs. σ_{xx} for strained NIO-227 thin films with different amounts of IrO_2 ablation at H_{ext} = 0 T. The straight red dotted line features the $\sigma_{xx}^{1.6}$ dependence of σ_{xy}^{AHE}, indicating the intrinsic origin of σ_{xy}^{AHE}.

3.4 Conclusion

In summary, we systematically investigated the impact of IrO_2 ablation on the structural inhomogeneity and related magnetotransport in strained NIO-227 films. By controlling the amount of IrO_2 ablation through the RRHSE method, we were able to regulate structural inhomogeneity in the films. As a result, the improvement in electrical transport and AHE properties were observed, reflecting an increase in sample quality of pyrochlore iridate thin film.

As mentioned earlier, previous studies[27-40] on pyrochlore iridate thin films were primarily grown using the SPE method, which allowed for the synthesis of these films. However, most of the SPE-grown samples are either relaxed or partially strained, making it difficult to investigate strain-induced novel topological phenomena. In contrast, the RRHSE method enables the growth of fully-strained NIO-227 films. This allows for the exploration of strain-induced novel topological phenomena not only in NIO-227 but also in other members of the pyrochlore iridate family. Moreover, we can utilize the RRHSE method to investigate novel quantum phenomena in oxide materials that were hindered by growth difficulties. Thus, our study not only contributes to the understanding of the magnetotransport properties of NIO-227 films but also provides a valuable tool for exploring the rich physics of topological materials.

References

1. J. Wang and S. C. Zhang, *Nat Mater* **16** (11), 1062 (2017).
2. William Witczak-Krempa, Gang Chen, Yong Baek Kim, and Leon Balents, *Annual Review of Condensed Matter Physics* **5** (1), 57 (2014).
3. Jeffrey G. Rau, Eric Kin-Ho Lee, and Hae-Young Kee, *Annual Review of Condensed Matter Physics* **7** (1), 195 (2016).
4. Nicodemos Varnava and David Vanderbilt, *Physical Review B* **98** (24) (2018).
5. Bohm-Jung Yang and Yong Baek Kim, *Physical Review B* **82** (8) (2010).
6. K. Hwang and Y. B. Kim, *Sci Rep* **6**, 30017 (2016).
7. B. J. Yang and N. Nagaosa, *Phys Rev Lett* **112** (24), 246402 (2014).
8. Kai-Yu Yang, Yuan-Ming Lu, and Ying Ran, *Physical Review B* **84** (7) (2011).
9. Taekoo Oh, Hiroaki Ishizuka, and Bohm-Jung Yang, *Physical Review B* **98** (14) (2018).
10. William Witczak-Krempa, Ara Go, and Yong Baek Kim, *Physical Review B* **87** (15) (2013).
11. K. Ueda, J. Fujioka, C. Terakura, and Y. Tokura, *Physical Review B* **92** (12) (2015).
12. K. Ueda, R. Kaneko, H. Ishizuka, J. Fujioka, N. Nagaosa, and Y. Tokura, *Nat Commun* **9** (1), 3032 (2018).
13. K. Ueda, T. Oh, B. J. Yang, R. Kaneko, J. Fujioka, N. Nagaosa, and Y. Tokura, *Nat Commun* **8**, 15515 (2017).
14. K. Ueda, J. Fujioka, B. J. Yang, J. Shiogai, A. Tsukazaki, S. Nakamura, S. Awaji, N. Nagaosa, and Y. Tokura, *Phys Rev Lett* **115** (5), 056402 (2015).
15. Zhaoming Tian, Yoshimitsu Kohama, Takahiro Tomita, Hiroaki Ishizuka, Timothy H. Hsieh, Jun J. Ishikawa, Koichi Kindo, Leon Balents, and Satoru Nakatsuji, *Nature Physics* **12** (2), 134 (2015).

16. M. Nakayama, T. Kondo, Z. Tian, J. J. Ishikawa, M. Halim, C. Bareille, W. Malaeb, K. Kuroda, T. Tomita, S. Ideta, K. Tanaka, M. Matsunami, S. Kimura, N. Inami, K. Ono, H. Kumigashira, L. Balents, S. Nakatsuji, and S. Shin, *Phys Rev Lett* **117** (5), 056403 (2016).
17. T. Kondo, M. Nakayama, R. Chen, J. J. Ishikawa, E. G. Moon, T. Yamamoto, Y. Ota, W. Malaeb, H. Kanai, Y. Nakashima, Y. Ishida, R. Yoshida, H. Yamamoto, M. Matsunami, S. Kimura, N. Inami, K. Ono, H. Kumigashira, S. Nakatsuji, L. Balents, and S. Shin, *Nat Commun* **6**, 10042 (2015).
18. Woo Jin Kim, Jeongkeun Song, Yangyang Li, and Tae Won Noh, *APL Materials* **10** (8) (2022).
19. N. P Armitage, E. J Mele, and Ashvin Vishwanath, *Reviews of Modern Phys*ics **90** (1) (2018).
20. Xiang Hu, Andreas Rüegg, and Gregory A. Fiete, *Physical Review B* **86** (23) (2012).
21. Qi Chen, Hsiang-Hsuan Hung, Xiang Hu, and Gregory A. Fiete, *Physical Review B* **92** (8) (2015).
22. X. Hu, Z. Zhong, and G. A. Fiete, *Sci Rep* **5**, 11072 (2015).
23. P. Laurell and G. A. Fiete, *Phys Rev Lett* **118** (17), 177201 (2017).
24. T.H. Okabe K.T. Jacob, T. Uda, Y. Waseda, *Electrochimica Acta* **45**, 1963 (2000).
25. G. W. H ooper C. B. Alcock, *Proc. R. Soc. London. Ser. A. Math. Phys. Sci.* **254**, 551 (1960).
26. Woo Jin Kim, Eun Kyo Ko, So Yeun Kim, Bongju Kim, and Tae Won Noh, *Current Applied Physics* **19** (4), 400 (2019).
27. Lu Guo, Shun-Li Shang, Neil Campbell, Paul G. Evans, Mark Rzchowski, Zi-Kui Liu, and Chang-Beom Eom, *npj Computational Materials* **7** (1) (2021).

28. W. C. Yang, Y. T. Xie, W. K. Zhu, K. Park, A. P. Chen, Y. Losovyj, Z. Li, H. M. Liu, M. Starr, J. A. Acosta, C. G. Tao, N. Li, Q. X. Jia, J. J. Heremans, and S. X. Zhang, *Sci Rep* **7** (1), 7740 (2017).
29. J. C. Gallagher, B. D. Esser, R. Morrow, S. R. Dunsiger, R. E. Williams, P. M. Woodward, D. W. McComb, and F. Y. Yang, *Sci Rep* **6**, 22282 (2016).
30. T. C. Fujita, Y. Kozuka, M. Uchida, A. Tsukazaki, T. Arima, and M. Kawasaki, *Sci Rep* **5**, 9711 (2015).
31. T. C. Fujita, M. Uchida, Y. Kozuka, S. Ogawa, A. Tsukazaki, T. Arima, and M. Kawasaki, *Applied Physics Letters* **108** (2) (2016).
32. Woo Jin Kim, John H. Gruenewald, Taekoo Oh, Sangmo Cheon, Bongju Kim, Oleksandr B. Korneta, Hwanbeom Cho, Daesu Lee, Yoonkoo Kim, Miyoung Kim, Je-Geun Park, Bohm-Jung Yang, Ambrose Seo, and Tae Won Noh, *Physical Review B* **98** (12) (2018).
33. Y. Li, T. Oh, J. Son, J. Song, M. K. Kim, D. Song, S. Kim, S. H. Chang, C. Kim, B. J. Yang, and T. W. Noh, *Adv Mater* **33** (25), e2008528 (2021).
34. T. C. Fujita, M. Uchida, Y. Kozuka, W. Sano, A. Tsukazaki, T. Arima, and M. Kawasaki, *Physical Review B* **93** (6) (2016).
35. T. C. Fujita, Y. Kozuka, J. Matsuno, M. Uchida, A. Tsukazaki, T. Arima, and M. Kawasaki, *Physical Review Materials* **2** (1) (2018).
36. Takumi Ohtsuki, Zhaoming Tian, Mario Halim, Satoru Nakatsuji, and Mikk Lippmaa, *Journal of Applied Physics* **127** (3) (2020).
37. T. Ohtsuki, Z. Tian, A. Endo, M. Halim, S. Katsumoto, Y. Kohama, K. Kindo, M. Lippmaa, and S. Nakatsuji, *Proc Natl Acad Sci U S A* **116** (18), 8803 (2019).

38. Lu Guo, Neil Campbell, Yongseong Choi, Jong-Woo Kim, Philip J. Ryan, Huaixun Huyan, Linze Li, Tianxiang Nan, Jong-Hong Kang, Chris Sundahl, Xiaoqing Pan, M. S. Rzchowski, and Chang-Beom Eom, *Physical Review B* **101** (10) (2020).
39. Xiaoran Liu, Fangdi Wen, E. Karapetrova, J. W. Kim, P. J. Ryan, J. W. Freeland, M. Terilli, T. C. Wu, M. Kareev, and J. Chakhalian, *Applied Physics Letters* **117** (4) (2020).
40. X. Liu, S. Fang, Y. Fu, W. Ge, M. Kareev, J. W. Kim, Y. Choi, E. Karapetrova, Q. Zhang, L. Gu, E. S. Choi, F. Wen, J. H. Wilson, G. Fabbris, P. J. Ryan, J. W. Freeland, D. Haskel, W. Wu, J. H. Pixley, and J. Chakhalian, *Phys Rev Lett* **127** (27), 277204 (2021).
41. Woo Jin Kim Taekoo Oh, Jeongkeun Song, Eun Kyo Ko, Yangyang Li, Bongju Kim Junsik Mun, Jaeseok Son, Zhuo Yang, Yoshimitsu Kohama, and Bohm-Jung Yang Miyoung Kim, Tae Won Noh, *Science Advances* **6** (eabb1539) (2020).
42. J. Song, T. Oh, E. K. Ko, J. H. Lee, W. J. Kim, Y. Zhu, B. J. Yang, Y. Li, and T. W. Noh, *Nat Commun* **13** (1), 6501 (2022).
43. A. W. Sleight and A. P. Ramirez, *Solid State Communications* **275**, 12 (2018).

Chapter 4

Higher harmonics in planar Hall effect induced by cluster multipoles

4.1 Introduction

The anomalous Hall effect (AHE) is a fundamental transport phenomenon that has been universally observed in time-reversal symmetry-broken systems. Conventionally, AHE has been observed mostly in itinerant ferromagnets. Its magnitude is known to be proportional to magnetization, which is a measure of broken time-reversal symmetry. Recently, a large AHE has been unexpectedly found in noncollinear antiferromagnets, such as Mn_3X (X = Sn, Ge) and GdPtBi, which do not exhibit spontaneous magnetization. Later, a similar AHE was observed in strained NIO-227 film. Importantly, the main mechanism This unconventional response indicates that ferromagnetism is not a necessary condition for AHE and suggests a possible alternative origin of AHE. In this chapter, I will discuss and demonstrate the relation between anomalous magnetotransport phenomena such as AHE and planar Hall effect and antiferromagnetic spin texture.

Part of Chapter 4 is published on Nature Comm. **13(1),** 6501 (2022)

4.1.1 Antiferromagnet

Antiferromagnetic (AFM) materials have attracted considerable interest as promising materials for next-generation spintronics[1-5] and novel topological phenomena[6-11]. This interest is largely due to the fact that the AFM spin arrangement produces zero net magnetization, leading to an absence of stray fields and insensitivity to external magnetic fields[12-13]. Additionally, the spin precession for AFM order is much faster than that in ferromagnets[14]. The resonance frequencies in antiferromagnets are in the terahertz range[15-17], whereas those of ferromagnets are in the gigahertz range. In parallel with AFM spintronics, antiferromagnets with topologically protected states have become another focus of recent interest. As AFM spin order breaks the time-reversal symmetry (TRS) or inversion symmetry, various topologically nontrivial states, including the Weyl semimetal[6-8], axion insulator[9-10], and Möbius insulator[11] can theoretically emerge.

4.1.2 Cluster magnetic multipoles

To develop novel AFM spintronics and investigate topological states in AFM materials, understanding the relationship between the spin texture and emergent phenomena in AFM materials is essential. This relationship can be theoretically described by the recently introduced cluster multipole theory (CMT)[18]. In CMT[18], magnetic structures are classified as "cluster multipoles" (dipole and additional high-rank multipoles) according to irreducible representations of the crystallographic point group. These cluster multipoles can be regarded as order parameters that reflect symmetry breaking in AFM materials. In particular, some cluster magnetic octupole (CMO) (i.e., T_1 octupole) belongs to the same magnetic point group (-42'm') as the magnetic dipole[18], leading to symmetry breaking and generating nonvanishing Berry curvature. In fact, the analysis using CMOs has been recently extended to understanding the large response of AHE[18-21], magneto-optical signals[22], the SHE[23-25], the anomalous Nernst effect[26-28], and perpendicular magnetization[29-30] in AFM materials. However, due to the absence of net magnetization, experimental identification of the CMOs in AFM materials is very challenging. To date, it has been limited to X-ray magnetic circular dichroism measurements[31] and the neutron scattering technique[32].

4.1.3 Three different kinds of cluster multipoles in pyrochlore iridate thin film

Since the deformation modulates magnetic anisotropy, the Ir spin directions should be changed. To systematically describe the change of spin direction, we adopted the cluster multipole theory. Since the conduction electrons come from Ir d-orbitals, we considered Ir sublattice only. In the cubic pyrochlore lattice, all spin ordering patterns can be classified into five different irreducible representations, carrying 12 distinct cluster multipoles. According to CMT, the AIAO ordering of bulk NIO-227 is equivalent to the A_2-CMO. This A_2- CMO breaks the TRS and generates nonvanishing Berry curvature, resulting in topological properties in momentum space such as the magnetic Weyl semimetal and Axion insulator.

4.2 Magnetotransport: anomalous Hall effect and planar Hall effect

The anomalous Hall effect (AHE) is a fundamental transport phenomenon that has been universally observed in time-reversal symmetry broken systems. AHE can arise from two different forms of mechanism: extrinsic mechanisms, such as skew scattering or side jump due to magnetic impurities, and intrinsic mechanism, originating from Berry curvature in momentum space. Since the fundamental topological properties of electronic wave functions are encoded in the Berry curvature, AHE is considered a powerful tool for probing the topological properties of materials. In addition to its fundamental interest, AHE can be applied to memory devices.

The planar Hall effect (PHE) has been considered a method of probing the physical properties of materials such as magnetism and topology. The PHE corresponds to the

development of a Hall voltage when electric and magnetic fields are coplanar, which is different from the usual Hall effect where they are perpendicular to each other. Initially, the PHE was observed in ferromagnetic systems [33-36], detecting the anisotropic magnetization of ferromagnetic materials. Additionally, the PHE has recently been in the spotlight due to its role in detecting topological characteristics such as the chirality arising from Weyl fermions in magnetic Weyl semimetals[37-40]. The associated PHE in both ferromagnets and Weyl semimetals exhibit sin (2ϕ) or second harmonic PHE oscillations. In contrast, higher harmonics PHE oscillations beyond second in topological systems[41-44] have been recently reported, in which higher harmonics PHE originated from additional unknown parameters in materials.

Among many kinds of AFM materials, the family of *5d* AFM materials $R_2Ir_2O_7$ (*R*: rare-earth ions: Eu, Y, Nd, and Pr) has received considerable attention due to a plethora of intriguing properties[6-7]. The crystal structure of NIO-227 is composed of Ir and Nd tetrahedral sublattices (Fig. 4.1a), which have a symmetry identical to that of the diamond lattice. Most $R_2Ir_2O_7$ bulk compounds exhibit an intriguing spin configuration called all-in-all-out (AIAO). According to CMT, the AIAO ordering of bulk $R_2Ir_2O_7$ is equivalent to the A_2-CMO[21,45]. This A_2-CMO breaks the TRS and generates nonvanishing Berry curvature, resulting in topological properties in momentum space such as the magnetic Weyl semimetal[6] and Axion insulator[6].

Here, we demonstrate the detection and identification of CMO in fully-strained AFM $Nd_2Ir_2O_7$ (NIO-227) film via the PHE. Under epitaxial strain, three kinds of cluster multipoles (dipoles and A_2- and T_1-CMOs) can be induced in the NIO-227 film. By rotating the magnetic field, distinctive harmonics in the PHE oscillation were observed. Specifically, the dipole induces the second harmonic due to longitudinal magnetization (Fig. 1c), whereas the A_2- and T_1-CMO induce fourth and sixth harmonics in the PHE oscillation, respectively. We demonstrate that the higher harmonics of the PHE oscillation for both CMOs originate from

the magnetic response of the CMOs, called orthogonal magnetization (OM) (Fig.1d). Furthermore, cluster multipoles induce nonlinear magnetic field-dependent the planar Hall conductivity. This nonlinear magnetic field behavior of the planar Hall conductivity can be understood in terms of the magnetic properties of the cluster magnetic dipole and CMOs.

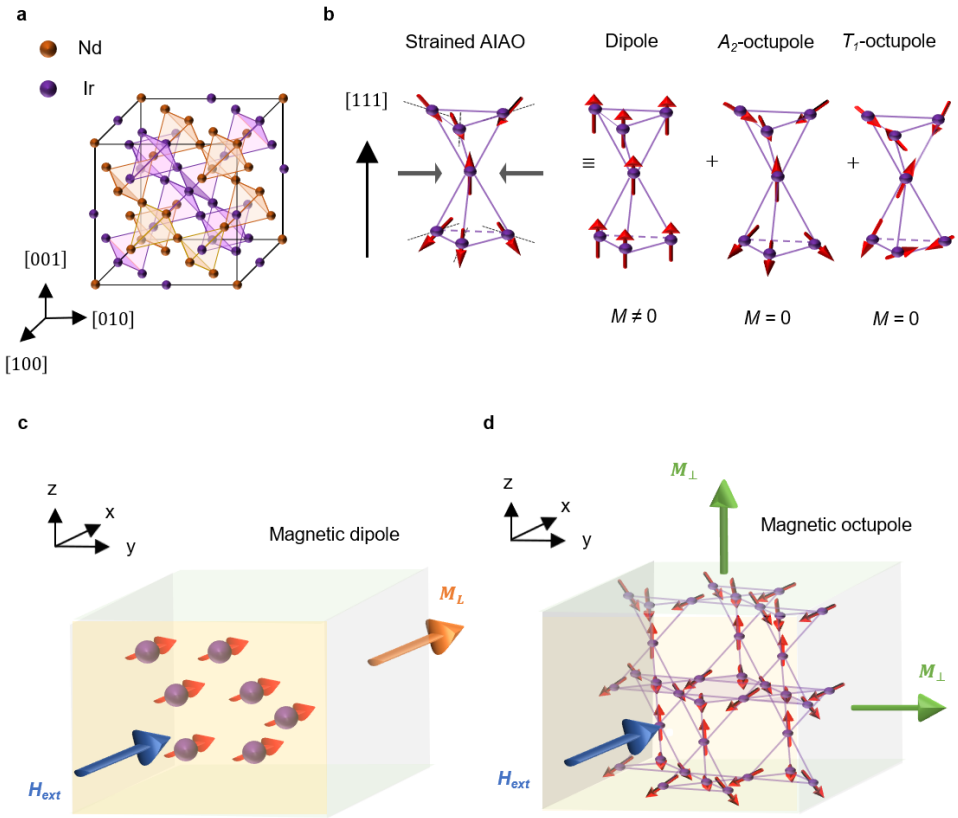

Figure 4.1 Schematic diagram of strain-induced cluster magnetic multipoles and OM in $Nd_2Ir_2O_7$ thin films. a. Schematic view of the pyrochlore lattice structure of $Nd_2Ir_2O_7$. b. When compressive strain is applied to $Nd_2Ir_2O_7$ along the [111] direction, the AIAO configuration of the magnetic spin experiences spin canting. Such canting can be represented by three distinctive magnetic multipoles (dipole, A_2-octupole, and T_1-octupole). Note that the dipole has finite magnetization, whereas the A_2-octupole and T_1-octupole do not have magnetization. c. Schematic diagram of the longitudinal magnetization induced by the dipole. When H_{ext} is applied along the x-y plane, the spin direction is aligned in the direction of H_{ext}. d. Schematic diagram of the OM induced by coupling between an external magnetic field (H_{ext}) and magnetic octupoles. The OM can be induced in two directions: normal to the surface and in-plane.

To investigate the magnetotransport properties of CMOs, we fabricated 15 nm fully strained NIO-227 films on a (111)-oriented yttria-stabilized zirconia (YSZ) substrate. Figure 4.2a shows the X-ray diffraction (XRD) pattern of a (111)-oriented NIO-227 thin film on a YSZ substrate. The strong odd-pair peaks in the XRD pattern exhibit excellent crystallization of the pyrochlore phase in the NIO film. Further analysis of the reciprocal space map (Fig. 4.2b) shows that the NIO-227 film is fully strained with a compressive strain of ~ 1 %. As mentioned earlier, the presence of compressive strain in the NIO-227 film is crucial, as it modulates the AIAO ordering and develops T_1-CMOs. Figure 4.2c shows the longitudinal resistivity ρ_{xx} *(T)* of the NIO-227 thin film as a function of temperature without a magnetic field. Clearly, with decreasing *T*, the NIO-227 film exhibits stronger semimetallic behavior than that of bulk NIO-227. At $T \sim 2$ K, our NIO-227 film has a ρ_{xx} of ~ 2.28 mΩ cm, whereas that of bulk NIO-227 is ~ 2.20×10^3 mΩ cm[46]. With compressive strain, the valence and conduction bands move in the NIO-227 film. The valence and conduction bands cross near the Fermi level, resulting in the development of electron and hole pockets[21]. These previous model calculations explain the enhancement of the conductivity in the NIO-227 thin film compared to the bulk.

Moreover, the AHE ($\sigma_{xy}^{AHE}(H)$) of the NIO-227 film was measured with H_{ext} applied along the [111] direction below 30 K. As shown in Fig. 4.2d, $\sigma_{xy}^{AHE}(H)$ at 2 K shows a hysteric feature with a finite value at 0 T, known as the spontaneous Hall effect[21]. In our strained NIO-227 thin film, the AHE and spontaneous Hall effect developed below 30 and 15 K, respectively. The value of the spontaneous Hall effect approached the maximum value at 2 K. The appearance of AHE below 30 K was previously attributed to Ir spin ordering[21]. In contrast, the emergence of the spontaneous Hall effect without magnetization below 15 K in the NIO-227 film is known to be the nontrivial contribution of the T_1-CMO to the Berry curvature[21], which is amplified by Nd ordering through *f-d* exchange interaction. In our 15 nm NIO-227 film, the

spontaneous Hall effect is observed without magnetization, which is induced by T_1-CMO in the film.

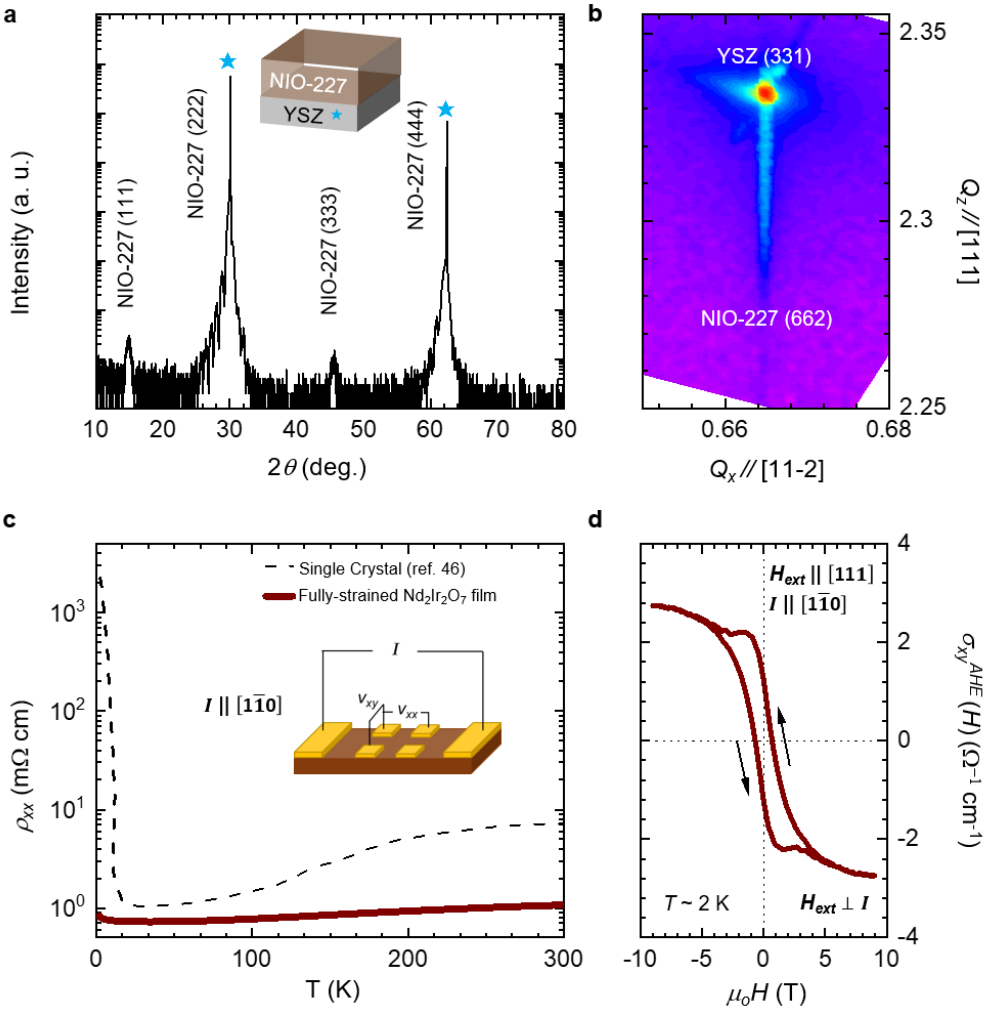

Figure. 4.2 Characterization of a $Nd_2Ir_2O_7$ thin film. a. High-resolution XRD pattern of a 15 nm thick $Nd_2Ir_2O_7$ (NIO-227) thin film. The NIO-227 thin film was grown on a YSZ substrate. b. Reciprocal space map of the NIO-227 film in the vicinity of the YSZ (331) reflection, indicating that the NIO-227 film is fully strained. c. The plot of the longitudinal resistivity, ρ_{xx}, vs. temperature, T, of NIO-227 thin film and single crystal (Ref. 46 in the main manuscript). d. The AHE is measured by applying H_{ext} along the [111] direction and I along the [1$\bar{1}$0] direction at 2 K. A clear AHE without a magnetic field is the signature of the presence of the T_1-octupole in the NIO-227 thin film.

To detect CMOs in the NIO-227 film, we performed PHE measurements. As shown in Fig. 4.3a, the PHE ($\Delta\sigma_{xy}^{PHE}(\phi,\ H\ = \pm 9\ \mathrm{T})$) below 30 K was measured across the width of the sample by applying I along the $[1\bar{1}0]$ direction with the rotation of H_{ext}. Magnetotransport properties were measured via a standard four-point probe method using a commercial physical property measurement system (PPMS; Quantum Design Inc., San Diego, CA, USA), which has a base T of 2 K and a maximum magnetic field of 9 T. Au layer (thickness: ~50 nm) was deposited by an e-beam evaporator on the NIO-227 film and used as an electrode. For the AHE measurement, the current was applied along the $[1\bar{1}0]$ direction, while H was applied in the [111] direction. For the PHE measurement, the current was applied along the $[1\bar{1}0]$ direction and H was rotated between the $[1\bar{1}0]$ and $[11\bar{2}]$ directions. The R_{xy} and longitudinal magnetoresistance R_{xx} below 30 K were simultaneously measured while varying ϕ and fixing H_{ext} at $\pm$ 9 T. The out-of-plane contribution of H_{ext} caused by a slight misalignment of the electrode can be removed by symmetrizing the R_{xy} acquired at +9 and –9 T. Then, the planar Hall conductivity σ_{xy}^{PHE} is calculated by $\sigma_{xy}^{PHE} = \frac{-\rho_{xy}^{PHE}}{\rho_{xy}^{PHE^2}+\rho_{xx}{}^2}$ and normalized ($\Delta\sigma_{xy}^{PHE}(\phi)$); here, $-\rho_{xy}^{PHE} and\ \rho_{xx}$ are the PHE resistivity and longitudinal resistivity, respectively.

In the range of 15-30 K, the $\Delta\sigma_{xy}^{PHE}(\phi)$ curves in the NIO-227 film mostly exhibit sin (2ϕ) oscillations (Fig. 3b). The sin (2ϕ) behavior (second harmonic) of the $\Delta\sigma_{xy}^{PHE}(\phi)$ oscillation above 15 K can be understood as the magnetization from dipolar order. As shown in Fig. 4.1b, the NIO-227 film has a cluster dipole, which can be regarded as ferromagnetic ordering. This cluster dipole induces M_L to be directed along H_{ext}, which can result in the second harmonic of the $\Delta\sigma_{xy}^{PHE}(\phi)$ oscillation. Thus, the second harmonic of the $\Delta\sigma_{xy}^{PHE}(\phi)$ oscillation above 15 K can be understood as the transverse voltage developed by the cluster dipole in the NIO-227 film under H_{ext}.

Below T ~ 15 K, the behavior of the $\sigma_{xy}^{PHE}(\phi)$ curves are complex but periodic, exhibiting oscillations of multiple harmonics. As shown in Fig. 4.3b, the $\Delta\sigma_{xy}^{PHE}(\phi)$ oscillation at 2 K cannot be explained only by the typical second harmonic induced by dipolar order. Such complex behavior of the $\Delta\sigma_{xy}^{PHE}(\phi)$ oscillation can be seen in the contour plot presented in Fig 4.3c. Whereas the second harmonic of $\Delta\sigma_{xy}^{PHE}(\phi)$ (green region) exists in all temperature regions below 30 K, additional harmonics (red region) of the $\Delta\sigma_{xy}^{PHE}(\phi)$ oscillation appears below 15 K. As a result, the $\Delta\sigma_{xy}^{PHE}(\phi)$ curve exhibits oscillations of multiple harmonics below 15 K.

To obtain further insight into the anomalous behavior of $\sigma_{xy}^{PHE}(\phi)$ curves below 15 K, we performed a fast Fourier transform (FFT) of the measured $\sigma_{xy}^{PHE}(\phi)$ curves. The FFT was performed to observe the ω dependence of the $\sigma_{xy}^{PHE}(\phi)$ curves below 30 K. As an example, to demonstrate the FFT process, the 2 K $\sigma_{xy}^{PHE}(\phi)$ curve is used (Fig. 4.4a). Then, we converted ϕ into radians, and repetition of the $\sigma_{xy}^{PHE}(\phi)$ curve was performed to increase the accuracy of the FFT data (Fig. 4.4b). Then, the FFT was performed by using the FFT function in the Origin program.

The harmonics (n) dependency of the FFT intensity in the $\Delta\sigma_{xy}^{PHE}(\phi)$ oscillation is shown in Fig. 4.3d. At 30 K, the second harmonic always exists, which is induced by the cluster dipole. The additional higher harmonics appear below 30 K. The appearance of the fourth harmonic in the $\Delta\sigma_{xy}^{PHE}(\phi)$ oscillation has been attributed to the A_2-CMO-induced chiral anomaly in $Pr_2Ir_2O_7$ thin films[41]. Considering that both $Pr_2Ir_2O_7$ and NIO-227 films have the A_2-CMO, the observed fourth harmonic of the $\Delta\sigma_{xy}^{PHE}(\phi)$ oscillation in the NIO-227 film

should originate from the A_2-CMO. However, the appearance of the sixth harmonic below 15 K (inset in Fig. 4.3d) cannot be explained by either the dipole or A_2-CMO.

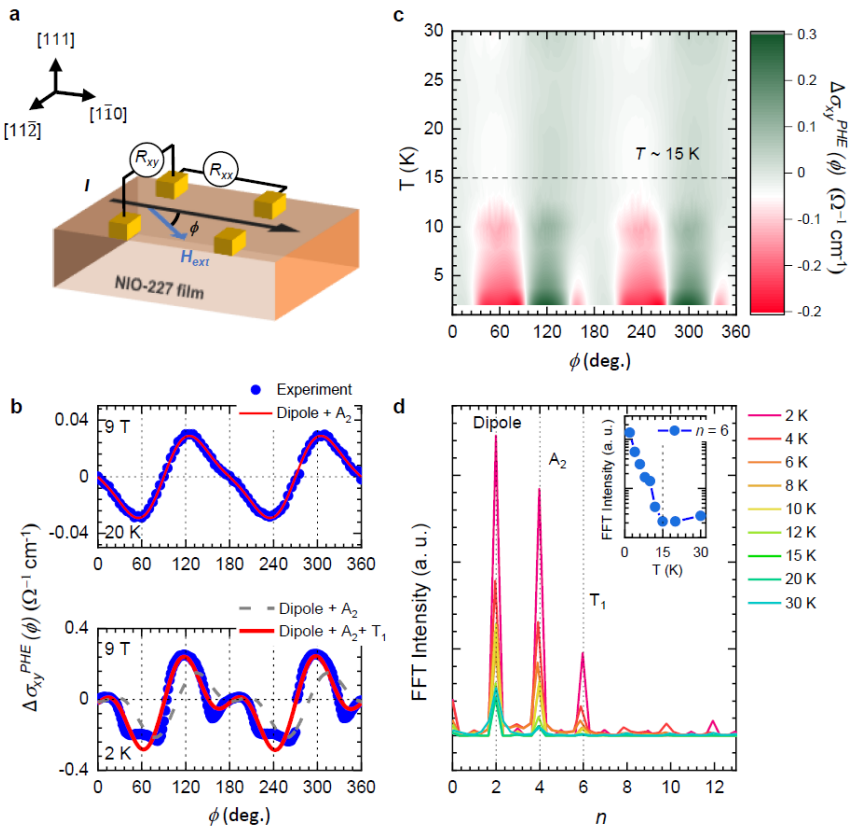

Figure. 4.3 Anomalous magnetic oscillation in the $\Delta\sigma_{xy}^{PHE}(\phi,\ H\ = \pm 9$ T) of the NIO-227 thin film. a. Schematic diagram of the $\Delta\ \sigma_{xy}^{PHE}(\phi)$ measurement geometry. In this geometry, I is applied along the [1 $\bar{1}$ 0] direction and H_{ext} is rotated within the sample plane. b. $\Delta\ \sigma_{xy}^{PHE}(\phi)$ curves at 20 and 2 K. At 20 K, the $\Delta\ \sigma_{xy}^{PHE}(\phi)$ curve has a sin (2ϕ) oscillation. c. Contour plot of all $\Delta\ \sigma_{xy}^{PHE}(\phi)$ curves below 30 K. d. FFT results of all $\Delta\ \sigma_{xy}^{PHE}(\phi)$ curves with different T. The FFT intensities of the second, fourth, and sixth harmonics are related to magnetization from the dipole, OM induced by the A_2-CMO, and OM induced by the T_1-CMO, respectively. The inset shows the temperature dependence of the sixth harmonic below 30 K.

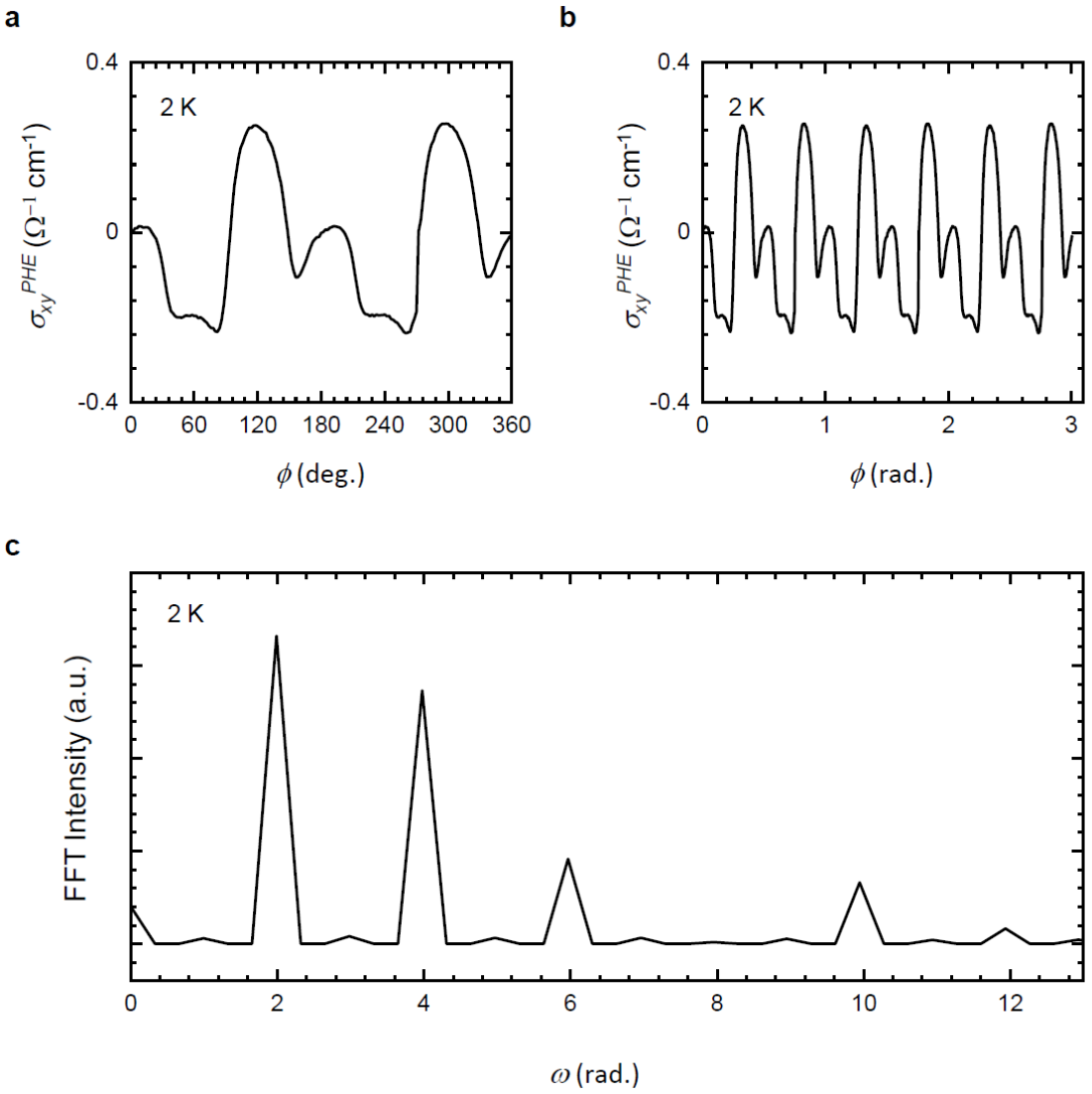

Figure 4.4 Process of fast Fourier transform of planar Hall effect curves. To see the dependency on each harmonic in the planar Hall effect curves, the fast Fourier transform was performed. a. The T ~ 2 K data of the planar Hall effect are shown to demonstrate the process of performing fast Fourier transforms in this work. b. The plot of the planar Hall effect was converted into radians. c. The plot of the performed fast Fourier transform.

4.3 Nonlinear planar Hall effect

To elucidate the appearance of the sixth harmonic in the $\Delta\sigma_{xy}^{PHE}(\phi)$ oscillation, we calculate $\Delta\sigma_{xy}^{PHE}$ from the dipole and A_2- and T_1-CMOs using the phenomenological model. Notably, the A_2-CMO induces an unusual magnetic response perpendicular to H_{ext}. This magnetic response was initially observed in a $Eu_2Ir_2O_7$ single crystal by torque magnetometry and defined as OM[30]. As mentioned above, the T_1-CMO is also expected to exhibit OM. Employing the expression[30] of the OM in $Eu_2Ir_2O_7$, we obtained the ϕ dependence of $\Delta\sigma_{xy}^{PHE}(\phi)$ for our system, expressed as follows:

$$\Delta\sigma_{xy}^{PHE}(\phi) = \sigma_{xy}^{Dipole} + \sigma_{xy}^{A2} + \sigma_{xy}^{T1} = A\sin(2\phi) + B\sin(4\phi) + C\sin(6\phi), \quad (1)$$

where A is the PHE coefficient of the dipole. B and C are the PHE coefficients of the OM induced by A_2- and T_1-CMOs, respectively. The detailed theoretical derivation is discussed in later section. Then, Eq. (1) can explain the appearance of peaks of the second, fourth, and sixth harmonics (Fig. 4.3d) by the M_L induced by the dipole, OM induced by the A_2-CMO, and OM induced by the T_1-CMO, respectively. In the range of 15-30 K, the $\Delta\sigma_{xy}^{PHE}(\phi)$ oscillation can be fitted with the M_L and OM induced by the dipole and A_2-CMO, respectively. The fitting of the $\Delta\sigma_{xy}^{PHE}(\phi)$ oscillation at 20 K without the sin (6ϕ) term in Eq. (1) is shown in Fig. 4.3b. This indicates that the cluster dipole and A_2-CMO of Ir spin ordering induce second and fourth harmonics of the $\Delta\sigma_{xy}^{PHE}(\phi)$ oscillation, respectively, while the contribution of the T_1-CMO is small in this temperature region.

In contrast, the $\Delta\sigma_{xy}^{PHE}(\phi)$ oscillation below 15 K can only be fitted by including the T_1-CMO contribution. As shown in Fig. 4.3b, Eq. (1), by including the sin (6ϕ) term from the T_1-CMO (red), well fits $\Delta\sigma_{xy}^{PHE}(\phi)$ at 2 K. The temperature dependence of the fitting result is

consistent with the appearance of the sixth harmonic peak below 15 K in the NIO-227 film. The multiple harmonics of anisotropic magnetoconductivity and out-of-plane rotation magnetoconductivity are developed below 15 K. These complex behaviors can be explained by including the contribution of T_1-CMOs, which is amplified by Nd ordering through *f-d* exchange interaction[21]. Therefore, we can confirm that the higher harmonics of $\sigma_{xy}^{PHE}(\phi)$ originate from A_2- and T_1-CMOs via OM.

Since the OM is the coupling effect between CMOs and H_{ext} and is known to have an H-field dependence[30], the $\sigma_{xy}^{PHE}(H)$ of NIO-227 should exhibit behavior different from that of a ferromagnet. We measured $\Delta\sigma_{xy}^{PHE}(\phi = 45^{\circ}, H)$ below 30 K by fixing ϕ = 45° between I and H_{ext} (Fig. 4.4a). The $\Delta\sigma_{xy}^{PHE}(H)$ curves with respect to H_{ext} below 20 K are shown in Fig. 4.4b. In the range of 15–20 K, the values of the $\Delta\sigma_{xy}^{PHE}(H)$ curves remain near zero at H_{ext} = +9 and −9 T. However, below 15 K, the values of the $\Delta\sigma_{xy}^{PHE}(H)$ curves have finite values with increasing H_{ext} and reach $\Delta\sigma_{xy}^{PHE}(H = +9\ \mathrm{T}) \sim -1.103\ \Omega^{-1}\ \mathrm{cm}^{-1}$ at 2 K.

By considering the OM induced by the A_2-CMO and T_1-CMO, we calculated $\Delta\sigma_{xy}^{PHE}(H)$ using the phenomenological model. Based on our calculations, the relation of $\Delta\sigma_{xy}^{PHE}(H)$ to H_{ext} can be expressed as follows:

$$\Delta\sigma_{xy}^{PHE}(H) = a_2H^2 + a_3H^3 + a_4H^4 \qquad (2)$$

where a_2 is the coefficient of longitudinal magnetization induced by the dipole. Both a_3 and a_4 are the coefficients of OM induced by A_2- and T_1-CMOs. Figure 4.4c shows the fitting results for $\Delta\sigma_{xy}^{PHE}(H)$ at a selected temperature of ~ 4 K with (red line) and without (black dashed line) the H^3 and H^4 terms. The fitting with the OM contribution explains the experimental results better than that with the dipole, demonstrating the development of OM from H_{ext}. The

contribution of the PHE coefficients of a_2, a_3, and a_4 to $\Delta\sigma_{xy}^{PHE}(H)$ below 30 K is shown in Fig. 4.4d. Below 30 K, the dipole induces an H^2 dependence of $\Delta\sigma_{xy}^{PHE}(H)$ due to the longitudinal magnetization, as shown in Fig. 4.1c. In contrast, below 15 K, the contributions of a_2, a_3, and a_4 coexist. While dipolar order still affects $\Delta\sigma_{xy}^{PHE}(H)$, a_3 and a_4 may appear due to the OM induced by both the A_2 and T_1-CMOs. Through theoretical analysis and the PHE results, we confirm that the anomalous behavior of the PHE indeed originates from A_2- and T_1-CMOs. Our results summarizing the contributions to the AHE and PHE of the cluster magnetic dipole, A_2-CMO, and T_1-CMO are shown in Table 1.

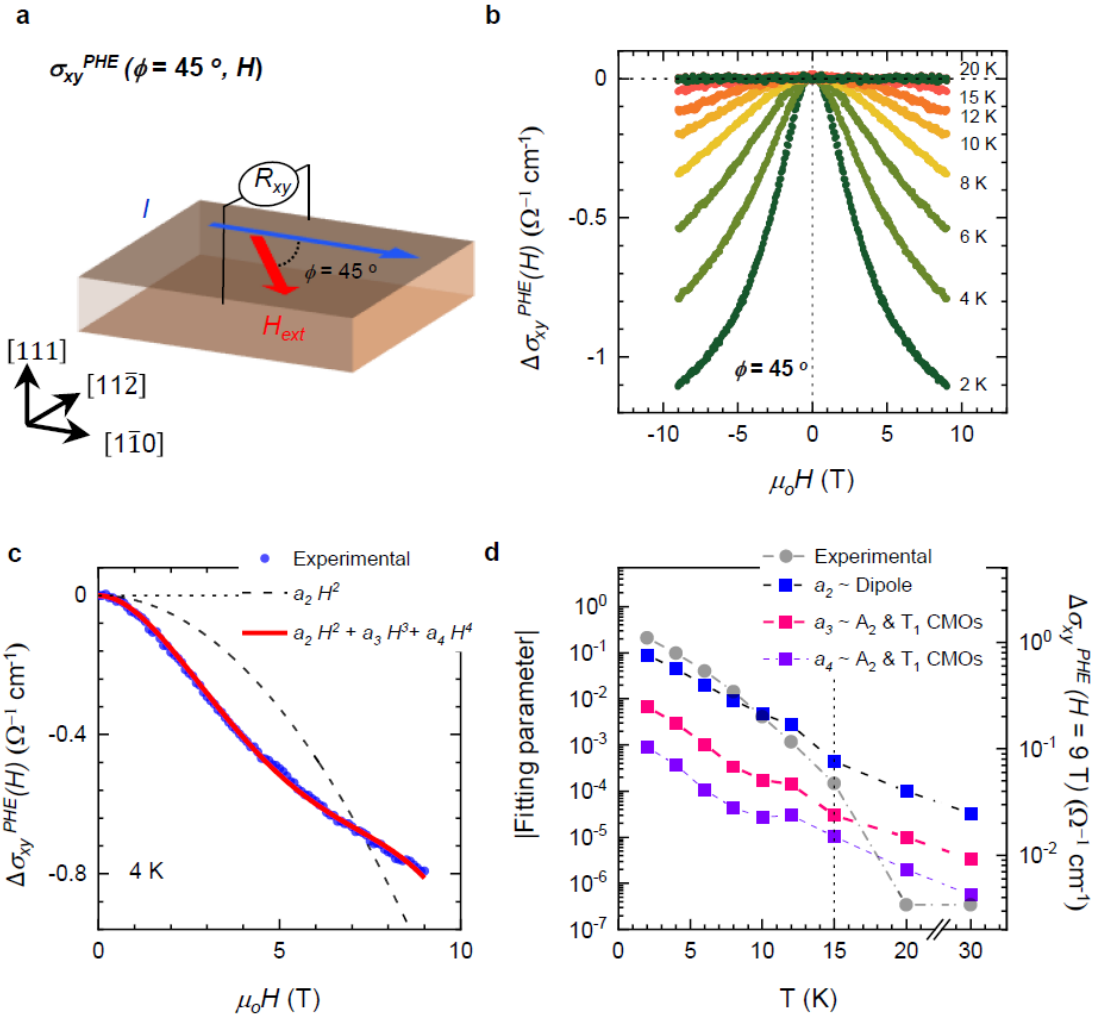

Figure 4.5 Nonlinear magnetic behavior of the $\Delta\sigma_{xy}^{PHE}(\phi = 45°, \mathrm{H})$ of the NIO-227 thin film. a. Schematic diagram of the $\Delta\sigma_{xy}^{PHE}(H)$ measurement geometry. b. $\Delta\sigma_{xy}^{PHE}(H)$ curves as a function of H_{ext} below T ~20 K. In the region of 15 K < T < 20 K, the value of $\Delta\sigma_{xy}^{PHE}(H)$is nearly zero. The slight deviation of $\Delta\sigma_{xy}^{PHE}(H)$ near $H_{ext} \sim \pm 9\ T$ at T ~15 K is possibly due to dipolar order. c. Logarithmic plot of the results of fitting $\Delta\sigma_{xy}^{PHE}(H)$ at T ~ 4 K with $\Delta\sigma_{xy}^{PHE}(H) = a_2H^2 + a_3H^3 + a_4H^4$ (red line). d. The plot of extracted fitting parameters a_2, a_3, and a_4 and $\Delta\sigma_{xy}^{PHE}(H = 9\ T)$ for the measured T.

	Dipole	A_2-octupole	T_1-octupole
M	$\neq 0$	$= 0$	$= 0$
$\sigma_{xy}^{AHE}(H)$ (ref. 2)	$\neq 0$	$= 0$	$\neq 0$
$M_{\perp}$	$= 0$	$\neq 0$	$\neq 0$
$\sigma_{xy}^{PHE}(\phi)$	second	fourth	sixth
$\sigma_{xy}^{PHE}(H)$	$\sim H^2$	$\sim H^3$ and $\sim H^4$	$\sim H^3$ and $\sim H^4$

Table 1 Contributions of magnetic orderings to the anomalous and planar Hall effects. Each contribution of magnetic orderings to the anomalous and planar Hall effects is shown. The contribution of T_1-octupole ordering to the $\sigma_{xy}^{AHE}(H)$ of the $Nd_2Ir_2O_7$ thin film can induce a finite $\sigma_{xy}^{AHE}(H = 0)$[2]. In contrast, the orthogonal magnetization, $M_{\perp}$, is induced from cluster magnetic octupoles, affecting $\sigma_{xy}^{PHE}(\phi)$ and $\sigma_{xy}^{PHE}(H)$ with distinctive features.

4.4 Theoretical derivation of orthogonal magnetization from magnetic octupole ordering and its effect on the planar Hall effect.

Results from the Hubbard model for pyrochlore iridates

The Hubbard model for pyrochlore iridates is

$$H = H_0 + H_U + H_B, \tag{1}$$

where H_0 is the hopping Hamiltonian, H_U is the Hubbard repulsion, and H_B is the Zeeman term. Specifically,

$$\begin{aligned} \mathrm{H}_0 &= \sum_{\langle ij\rangle} c_{i\alpha}^{+}\alpha_{ij}(\delta)\left(t_1 + it_2\,\overrightarrow{d_{\iota J}}\times\vec{\sigma}_{\alpha\beta}\right)c_{j\beta} \\ &\quad + \sum_{\langle\langle ij\rangle\rangle} c_{i\alpha}^{+}\left(t_3 + i\left(t_4\overrightarrow{R_{\iota J}} + t_5\overrightarrow{D_{\iota J}}\right)\times\vec{\sigma}_{\alpha\beta}\right)c_{j\beta}, \\ \mathrm{H}_\mathrm{U} &= U\sum_i n_{i\uparrow}n_{i\downarrow}, \\ \mathrm{H}_\mathrm{B} &= -\vec{B}\cdot\sum_i c_{i\alpha}^{+}\vec{\sigma}_{\alpha\beta}c_{i\beta}, \end{aligned} \tag{2}$$

where $\mathrm{t}_{1,2,3,4,5}$ are the hopping parameters as a function of super-exchange hopping $\mathrm{t}_{\mathrm{oxy}}$, $\alpha_{ij}(\delta)$ is the change in the hopping parameters induced by strain, $\overrightarrow{d_{\iota J}}$ $\left(\overrightarrow{R_{\iota J}}, \overrightarrow{D_{\iota J}}\right)$ are the nearest (next-nearest) Dzyaloshinskii-Moriya (DM) vectors, and $\vec{\sigma}$ is the vector of Pauli matrices. The hopping parameters are defined as

$$
\begin{aligned}
t_1 &= \frac{130}{243} + \frac{17}{324} t_\sigma - \frac{79}{243} t_\pi, \\
\mathrm{t}_2 &= \frac{28}{243} + \frac{15}{243} t_\sigma - \frac{40}{243} t_\pi, \\
\mathrm{t}_3 &= \frac{233}{2916} t'_\sigma - \frac{407}{2187} t'_\pi, \\
\mathrm{t}_4 &= \frac{t'_\sigma}{1458} + \frac{220}{2187} t'_\pi, \\
\mathrm{t}_5 &= \frac{25}{1458} t'_\sigma + \frac{460}{2187} t'_\pi.
\end{aligned} \tag{3}
$$

where $\mathrm{t}_\sigma = -0.8 t_{oxy}, t_\pi = -\frac{2}{3} t_\sigma, t'_\sigma = 0.08 t_\sigma,$ and $t'_\pi = 0.08\, t_\pi$. We set $\mathrm{t}_{\mathrm{oxy}} = 1$. The change in the hopping parameters is defined as

$$
\alpha_{ij}(\delta) = \begin{cases} 1 - \delta \ (\mathrm{ij} = 12,13,14). \\ 1 + \delta \ (ij = 23,24,34). \end{cases} \tag{4}
$$

The DM vectors are defined as

$$
\begin{aligned}
\overrightarrow{d_{\iota J}} &= 2\overrightarrow{f_{\iota J}} \times \vec{x}_{ij}, \\
\overrightarrow{R_{\iota J}} &= \vec{x}_{ik} \times \vec{x}_{kj}, \\
\overrightarrow{D_{\iota J}} &= \overrightarrow{d_{\iota k}} \times \overrightarrow{d_{kJ}},
\end{aligned} \tag{5}
$$

where $\overrightarrow{x_{\iota J}} = \overrightarrow{x_J} - \overrightarrow{x_\iota}$ is the displacement between sites *i* and *j* and $\overrightarrow{f_{\iota J}}$ is the vector from the unit cell center to the bond center between sites *i* and *j*.

The Hubbard repulsion is expressed in the mean-field approximation as

$$
\mathrm{H_U} \approx -U \sum_i \left(2\vec{J_\iota} \cdot \langle \vec{J_\iota} \rangle - \langle \vec{J_\iota} \rangle^2 \right), \tag{6}
$$

where $\vec{\mathrm{J}_\mathrm{i}} = \frac{1}{2} \sum_{\alpha\beta} c^+_{i\alpha} \vec{\sigma}_{\alpha\beta} c_{i\beta}$ is the spin operator. We set $\mathrm{U} = 1.485 t_{oxy}$ or $\mathrm{U} = 1.5 t_{oxy}$. Lastly, the magnetic field is applied in either the $[111]$ plane or the $[11\bar{2}]$ plane, That is,

$$\vec{B} = B\left(\frac{(1,-1,0)}{\sqrt{2}}\cos\phi + \frac{(1,1,-2)}{\sqrt{6}}\sin\phi\right),$$
$$\vec{B} = B\left(\frac{(1,-1,0)}{\sqrt{2}}\cos\theta + \frac{(1,1,1)}{\sqrt{3}}\sin\theta\right). \quad (7)$$

δ and B are variables. In the rest of this part, we change the basis to $\hat{x} \parallel [1\bar{1}0], \hat{y} \parallel [11\bar{2}]$, and $\hat{z} \parallel [111]$. Using the model, we self-consistently calculate the ground state of the Hubbard model with a $32 \times 32 \times 32$ *k*-mesh. The results are shown in Figs. s5. The blue solid line corresponds to the A_2-octupole, the orange dotted line to the T_{1x}-octupole, the orange circles to the T_{1y}-octupole, and the orange solid line to the T_{1z}-octupole. The definition of each multipole is

$$\begin{aligned} A_2 &= \frac{1}{4\sqrt{3}}\langle \sigma_{1x} + \sigma_{1y} + \sigma_{1z} + \sigma_{2x} - \sigma_{2y} - \sigma_{2z} - \sigma_{3x} + \sigma_{3y} - \sigma_{3z} - \sigma_{4x} \\ &\qquad - \sigma_{4y} + \sigma_{4z}\rangle, \\ T_{1x,o} &= \frac{1}{4\sqrt{2}}\langle -\sigma_{1y} - \sigma_{1z} + \sigma_{2y} + \sigma_{2z} + \sigma_{3y} - \sigma_{3z} - \sigma_{4y} + \sigma_{4z}\rangle, \\ T_{1y,o} &= \frac{1}{4\sqrt{3}}\langle -\sigma_{1x} - \sigma_{1z} + \sigma_{2x} - \sigma_{2z} + \sigma_{3x} + \sigma_{3z} - \sigma_{4x} + \sigma_{4z}\rangle, \\ T_{1z,o} &= \frac{1}{4\sqrt{3}}\langle -\sigma_{1x} - \sigma_{1y} + \sigma_{2x} - \sigma_{2y} - \sigma_{3x} + \sigma_{3y} + \sigma_{4x} + \sigma_{4y}\rangle, \end{aligned} \quad (8)$$

where $\langle \ldots \rangle$ is the expectation value. Since we change the basis, the T_1-octupoles transform as

$$T_{1x} = \frac{T_{1x,o} - T_{1y,o}}{\sqrt{2}},$$
$$T_{1y} = \frac{T_{1x,o} + T_{1y,o} - 2T_{1z,o}}{\sqrt{6}}, \quad (9)$$
$$T_{1z} = \frac{T_{1x,o} + T_{1y,o} + T_{1z,o}}{\sqrt{3}},$$

while A_2-octupole does not transform. Magnetization is defined as $\mathrm{M_a} = \sum_i \langle \sigma_{ia} \rangle$.

In Fig. 4.6, we show the emergence of T_1-octupoles under strain and a magnetic field. The ground state without δ and B is all-in-all-out (AIAO), which carries only the A_2-octupole.

When δ varies from 0 to 0.01 without B, T_{1z} appears and is proportional to δ. (See Fig. 4.6a.) Furthermore, when B varies from 0 to 0.02 with $\delta = 0.005$, T_{1x} and T_{1y} appear. (See Fig. 4.6b.) T_{1x} is proportional to B, while T_{1y} is proportional to B^2. Hence, the interplay of strain and the magnetic field induces T_1-octupoles.

In Fig. 4.7, we show the angular dependence of A_2- and T_1-octupoles. First, let us consider $\vec{B}$ in the [111] plane. When ϕ varies from 0 to 2π with $\delta = 0.005$, $U = 1.485t_{oxy}$, and $B = 0.02$ and $B = 0.02$, each order parameter has a distinct angular dependence. The A_2-octupole and T_{1z}-octupole have a $\sin 3\phi$ dependence, as shown in Fig. 4.7a. This is explained by the threefold rotation about the *z*-axis of the strained crystal. However, the T_{1x}-octupole and T_{1y}-octupole have $\cos\phi$ and $\sin\phi$ dependences, respectively. Next, let us consider $\vec{B}$ in the $[11\bar{2}]$ plane. When θ varies from 0 to 2π with $\delta = 0.01, U = 1.500t_{oxy}$, and $B = 0.02$, the order parameters show different angular dependence from above. A_2-octupole and T_{1z}-octupole depend on $\sin\theta$, while T_{1x} and T_{1y}-octupoles depend on $\cos\theta$ and $\cos 2\theta$, respectively. Since these T_1-octupoles have the same symmetry as the dipolar order or magnetization, T_{1x} and T_{1y} have the same angular dependence as the induced magnetization.

Orthogonal magnetization from the A_2-octupole and T_1-octupole

Although the A_2-octupole and T_1-octupole are magnetic octupoles, they are different for two reasons. The first reason is that the magnetic point groups of the A_2-octupole and T_1-octupole are different, $-4'3m'$ and $-42'm'$, respectively. $-4'3m'$ carries 3-fold rotation symmetries, while $-42'm'$ does not. The second reason is that the A_2-octupole is a scalar, while the T_1-octupole is a vector. Whether the order parameter is a scalar or vector changes how the magnetic field and octupoles are coupled to each other. Specifically, the free energy under a magnetic field $\vec{H}$ and A_2-octupole A_2 is given by

$$\mathrm{F_{A2}} = -A_2 H_x H_y H_z, \tag{10}$$

while the free energy under a magnetic field and $\mathrm{T_1}$-octupole $\overrightarrow{\mathrm{T_1}}$ is given by

$$\mathrm{F_{T1}} = -\overrightarrow{T_1} \cdot \vec{P}(\vec{H}), \tag{11}$$

where

$$P_i(\vec{H}) = -3H_i^3 + \frac{9}{2} H_i\left(H_j^2 + H_k^2\right). \tag{12}$$

Here, i, j, k is a cyclic permutation of x, y, z. Magnetization is the derivative of the free energy induced by a magnetic field. From the free energy of the $\mathrm{A_2}$-octupole, we obtain

$$M'_{A_2,i} = A_2 H_j H_k, \tag{13}$$

and from the free energy of the $\mathrm{T_1}$-octupole, we obtain

$$\begin{aligned} M'_{T_1,i} = T_{1i}\left(-9H_i^2 + \frac{9}{2}\left(H_j^2 + H_k^2\right)\right) + T_{1j}\left(9H_i H_j\right) \\ + T_{1k}(9H_i H_k). \end{aligned} \tag{14}$$

The components perpendicular to the magnetic field here are called orthogonal magnetization. Please note that this theory is for the small field limit.

From here, we change the basis to $\hat{x} \parallel [1\bar{1}0], \hat{y} \parallel [11\bar{2}]$, and $\hat{z} \parallel [111]$ for both the $\mathrm{T_1}$-octupole and magnetic field. The magnetic field is $\overrightarrow{\mathrm{H}} = \mathrm{H}(\cos\phi, \sin\phi, 0)$ in our physical situation. First, let us consider the magnetic field is in the *xy*-plane, i.e., $\overrightarrow{\mathrm{H}} = \mathrm{H}(\cos\phi, \sin\phi, 0)$. On this basis, the magnetization from the $\mathrm{A_2}$-octupole is

$$\begin{aligned} M_{A_2,x} &= -\frac{A_2}{\sqrt{6}} H^2 \sin 2\phi, \\ M_{A_2,y} &= -\frac{A_2}{\sqrt{6}} H^2 \cos 2\phi, \\ M_{A_2,z} &= -\frac{A_2}{2\sqrt{3}} H^2, \end{aligned} \tag{15}$$

and that from the $\mathrm{T_1}$-octupole is

$$
\begin{aligned}
M_{T_1,x} &= -\frac{3}{4}H^2\big(2\,T_{1x} + T_{1x}\cos 2\phi \\
&\qquad + \big(-5\sqrt{2}T_{1z} + T_{1y}\big)\sin 2\phi\big), \\
M_{T_1,y} &= \frac{3}{4}H^2\big(-2\,T_{1y} + \big(5\sqrt{2}\,T_{1z} + T_{1y}\big)\cos 2\phi \\
&\qquad - T_{1x}\sin 2\phi\big), \\
M_{T_1,z} &= \frac{3}{4}H^2\big(2\,T_{1z} + 5\sqrt{2}\,T_{1y}\cos 2\phi \\
&\qquad + 5\sqrt{2}\,T_{1x}\sin 2\phi\big).
\end{aligned} \tag{16}
$$

Next, let us consider the magnetic field is in the xz-plane, i.e., $\vec{\mathrm{H}} = \mathrm{H}(\cos\theta\,, 0, \sin\theta)$. The A_2-octupole gives

$$
\begin{aligned}
M_{A_2,x} &= -\frac{A_2}{2\sqrt{3}}H^2\sin 2\theta\,, \\
M_{A_2,y} &= \frac{A_2}{\sqrt{6}}H^2\cos^2\theta\,, \\
M_{A_2,z} &= -\frac{A_2}{4\sqrt{3}}H^2(-1 + 3\cos 2\theta),
\end{aligned} \tag{17}
$$

and T_1-octupole gives

$$
\begin{aligned}
M_{T_1,x} &= \frac{3}{8}H^2\big(\,T_{1x}(-1 + 7\cos 2\theta) \\
&\qquad - 2\big(5\sqrt{2}T_{1y} + 4T_{1z}\big)\sin 2\theta\big), \\
M_{T_1,y} &= \frac{3}{8}H^2\Big((-3 + 5\cos 2\theta)\,T_{1y} \\
&\qquad - 5\sqrt{2}\,(1 + \cos 2\theta)T_{1z} \\
&\qquad - 10\sqrt{2}T_{1x}\sin 2\theta\Big),
\end{aligned} \tag{18}
$$

$$M_{T_1,z} = -\frac{3}{4}H^2\left(-8\,T_{1z}\sin^2\theta + 4T_{1x}\sin 2\theta + \left(5\sqrt{2}\,T_{1y} + 4\,T_{1z}\right)\cos^2\theta\right).$$

Planar Hall conductivity from the A_2-octupole and T_1-octupole

The Onsager relation for the Hall conductivity is $\sigma_{ij}(\vec{H},\vec{M}) = \sigma_{ji}(-\vec{H},-\vec{M})$. The planar Hall conductivity is defined as the symmetric part of the Hall conductivity ($\sigma_{ij}(\vec{H},\vec{M}) = \sigma_{ji}(\vec{H},\vec{M})$). Specifically, the planar Hall conductivity (PHC) is

$$\sigma_{ij}^{P} = \sigma_0(H_iH_j) + \sigma_1(M_iH_j + M_jH_i) + \sigma_2(M_iM_j). \tag{19}$$

$\sigma_0, \sigma_1,$ and σ_2 are constants.

Here, we change the basis to $\hat{x} \parallel [1\bar{1}0]$, $\hat{y} \parallel [11\bar{2}]$, and $\hat{z} \parallel [111]$. Let us consider the magnetic field in the [111] plane, $\vec{\mathrm{H}} = \mathrm{H}(\cos\phi, \sin\phi, 0)$ The longitudinal magnetization (dipole) $\vec{M}_D = \chi\vec{H}$, and orthogonal magnetization $\overrightarrow{M_{A_2}}$ and $\overrightarrow{M_{T_1}}$. Note that the angular dependences of octupoles are $\mathrm{A}_2 \propto \sin 3\phi$, $T_{1x} \propto \cos\phi$, $T_{1y} \propto \sin\phi$, and $T_{1z} \propto \sin 3\phi$ from the Hubbard model.

We divide the PHC on the *xy*-plane σ_{xy}^{P} into three parts according to the origin. First, the PHC from $\vec{H}$ and $\overrightarrow{M_D}$ is given by

$$\sigma_{xy}^{P,M_D} \propto H^2 \sin 2\phi. \tag{20}$$

Second, the PHC from $\overrightarrow{M_{A_2}}$ and $\mathrm{A}_2 \propto \sin 3\phi$ is given by

$$\begin{aligned}\sigma_{\mathrm{xy}}^{P,A_2} = {} & H^3(a_1\cos\phi + a_2\sin 2\phi + a_3\sin 4\phi) \\ & + H^4(b_1\sin 2\phi + b_2\sin 4\phi \\ & + b_3\sin 10\phi),\end{aligned} \tag{21}$$

where a_i and b_i are constants. Third, the PHC from $\overrightarrow{M_{T_1}}$, $T_{1x} \propto \cos\phi$, $T_{1y} \propto \sin\phi$, and $T_{1z} \propto C + D\sin 3\phi$ is given by

$$\begin{aligned}\sigma_{xy}^{P,T_1} = {} & H^3(c_1\cos\phi + c_2\sin 2\phi + c_3\sin 4\phi) \\ & + H^4(d_1\cos\phi + d_2\sin 2\phi \\ & + d_3\sin 4\phi \\ & + d_4\sin 6\phi + d_5\sin 10\phi),\end{aligned} \tag{22}$$

where c_i and d_i are constants. Here, we note some points. First, $\sin 2\phi$ is dominated by σ_{xy}^{P,M_D} since it is proportional to the leading order H^2. Second, $\sin 4\phi$ is dominated by σ_{xy}^{P,A_2} since the A_2-octupole is the largest among all the order parameters. Third, $\sin 6\phi$ appears only in σ_{xy}^{P,T_1}. Hence, we denote $\sin 2\phi$ as the dipole term, $\sin 4\phi$ as the A_2-octupole term, and $\sin 6\phi$ as the T_1-octupole term.

$$\begin{aligned}\sigma_{xy}^{P,A_2} = {} & H^3(a_2\sin 2\phi + a_3\sin 4\phi) \\ & + H^4(b_1\sin 2\phi + b_2\sin 4\phi \\ & + b_3\sin 10\phi), \\ \sigma_{xy}^{P,T_1} = {} & H^3(c_2\sin 2\phi + c_3\sin 4\phi) \\ & + H^4(d_2\sin 2\phi + d_3\sin 4\phi \\ & + d_4\sin 6\phi + d_5\sin 10\phi).\end{aligned} \tag{23}$$

Using equations (19) and (22), we fitted the experimental planar Hall conductivity (Fig.s8).

We calculated the magnetization induced by strain and magnetic field in the octupolar system $Nd_2Ir_2O_7$ (Fig. 4.6). We recall that the planar Hall conductivity in $Nd_2Ir_2O_7$ is generated by the orthogonal magnetization that results from the coupling between the octopolar orders (higher-rank multipoles) and the magnetic field. Since orthogonal magnetization is the coupling between the higher rank multipoles and magnetic field, it should have small values. As expected (Fig. 4.6c and 4.6b), the magnetization (orthogonal magnetization) induced by the magnetic field in the strained $Nd_2Ir_2O_7$ is very small (at the scale of 10^{-3} μ_B/atom). Hence, the

octupolar contributions to the planar Hall conductivity are small.

Longitudinal magnetoconductivity from A_2 and T_1-octupoles

Meanwhile, we use Onsager's relation for longitudinal conductivity as well.

$$\sigma_{xx} = \sigma_0(H_x^2) + \sigma_1(M_x H_x) + \sigma_2(M_x^2). \tag{24}$$

First, let us consider the magnetic field in the [111] plane, $\vec{\mathrm{H}} = \mathrm{H}(\cos\phi, \sin\phi, 0)$, The obtained conductivity is anisotropic magnetoconductivity (AMC). The first term is

$$\sigma_{xx}^1 \propto \cos 2\phi, \tag{25}$$

$\overrightarrow{M_{A_2}}$ from A_2-octupole gives rise to

$$\begin{aligned}\sigma_{xx}^{\mathrm{A_2}} &= H^3(e_1 \sin\phi + e_2 \sin 3\phi) \\ &+H^4(f_1 \cos 2\phi + f_2 \cos 4\phi + f_3 \cos 6\phi \\ &\quad + f_4 \cos 10\phi),\end{aligned} \tag{26}$$

and $\overrightarrow{M_{T_1}}$ from T_1-octupole gives rise to

$$\begin{aligned}\sigma_{xx}^{\mathrm{T_1}} &= H^3(g_1 \sin\phi + g_2 \sin 3\phi + g_3 \cos 2\phi \\ &\quad + g_4 \cos 4\phi + g_5 \cos 6\phi) \\ &+H^4(h_1 \sin\phi + h_2 \sin 3\phi + h_3 \cos 2\phi \\ &\quad + h_4 \cos 4\phi + h_5 \cos 6\phi \\ &\quad + h_6 \cos 8\phi + h_7 \cos 10\phi).\end{aligned} \tag{27}$$

The experimental AMC for the measured temperature of $Nd_2Ir_2O_7$ film and the fitting result is shown in Fig. 4.8 and 4.9.

Next, let us consider the magnetic field in the $[11\bar{2}]$ plane, $\vec{\mathrm{H}} = \mathrm{H}(\cos\theta, 0, \sin\theta)$. The first term is

$$\sigma_{xx}^1 \propto \cos 2\theta, \tag{28}$$

$\overrightarrow{M_{A_2}}$ from A_2-octupole and $\overrightarrow{M_{T_1}}$ from T_1-octupole give rise to

$$\sigma_{xx} = H^3(x_1 \sin\theta + x_2 \sin 3\theta + \mathrm{x}_3 \sin 4\theta + x_4 \sin 5\phi \tag{29}$$

$$+H^4(y_1 \sin\theta + y_2 \sin 3\theta + y_3 \sin 5\phi + y_4 \cos 2\theta + y_5 \cos 4\theta + y_6 \cos 6\theta).$$

The experimental longitudinal magnetoconductivity with out-of-plane rotation for the measured temperature of $Nd_2Ir_2O_7$ film and the fitting result is shown in Fig. 4.10.

About the magnetic anisotropy of pyrochlore iridates

Ir spins have no magnetic anisotropy, although Ir is a *d*-electron system since Ir spins are considered spin-1/2. In the pyrochlore system, Ir ions are surrounded by an oxygen octahedron. Then, Ir *d*-orbitals are broken into t_{2g} and e_g orbitals by the crystal field. Moreover, Ir also has strong spin-orbit coupling, and t_{2g} is broken into $J = 1/2, 3/2$ orbitals. Because $J = 1/2$ is half-filled at the Fermi level, Ir spins are considered spin-1/2. In contrast, Nd spins have magnetic anisotropy along the [111] and equivalent axes because they have a high spin $J_{Nd} = 9/2$. In our free energy model, since we consider the magnetic order of Ir spins only, the magnetic anisotropy seems to be obviated.

However, most transport phenomena in pyrochlore iridates come from Ir *d* electrons and not from Nd *f* electrons since *f* electrons are strongly localized near the ionic center. Thus, the magnetic anisotropy of Nd *f* electrons can indirectly affect the transport by changing the Ir spin configuration through the *f-d* exchange. Since we study the magnetic multipole-induced planar Hall effect, considering the Ir spin configuration in the free energy model is sufficient to include the effect of magnetic anisotropy of Nd spins.

Furthermore, magnetic multipoles have already been considered for magnetic anisotropy. Here, the magnetic multipoles are made up of spin clusters in the unit cell. We classify every possible spin configuration into magnetic multipoles by group theory. There are a total of 12 magnetic multipoles since we have 4 atoms in the 3-dimensional unit cell: 3 dipoles, an A_2-octupole, 3 T_1-octupoles, 3 T_2-octupoles, and 2 E-dotriacontapoles. Every possible magnetic order can be expressed as a linear combination of the 12 magnetic multipoles. Meanwhile, magnetic anisotropy affects the spin configuration, either by making spins point along their easy axes or through the *f-d* exchange. The associated spin configuration can be described by the linear combination of magnetic multipoles. As the free energy contains the

coupling of magnetic multipoles to the magnetic field, our model includes the effect of magnetic anisotropy.

Lastly, we consider the effect of compressive strain on magnetic anisotropy. Magnetic anisotropy strongly depends on the temperature. In $Nd_2Ir_2O_7$, Ir spins order at 30 K, while Nd spins order at 15 K. Magnetic anisotropy becomes effective below 15 K, at which Nd spins order. However, compressive strain contributes little to magnetic anisotropy. The two largest energy scales that determine the physics in pyrochlore iridates are the energy gap between the t_{2g} and e_g orbitals (- 2 eV) and the spin-orbit coupling (-0.4 eV), which are much larger than the bandwidth. A compressive strain of approximately 1 %, in contrast, changes the band energy by a few percent of the bandwidth. Hence, the strain does not significantly change the magnetic anisotropy.

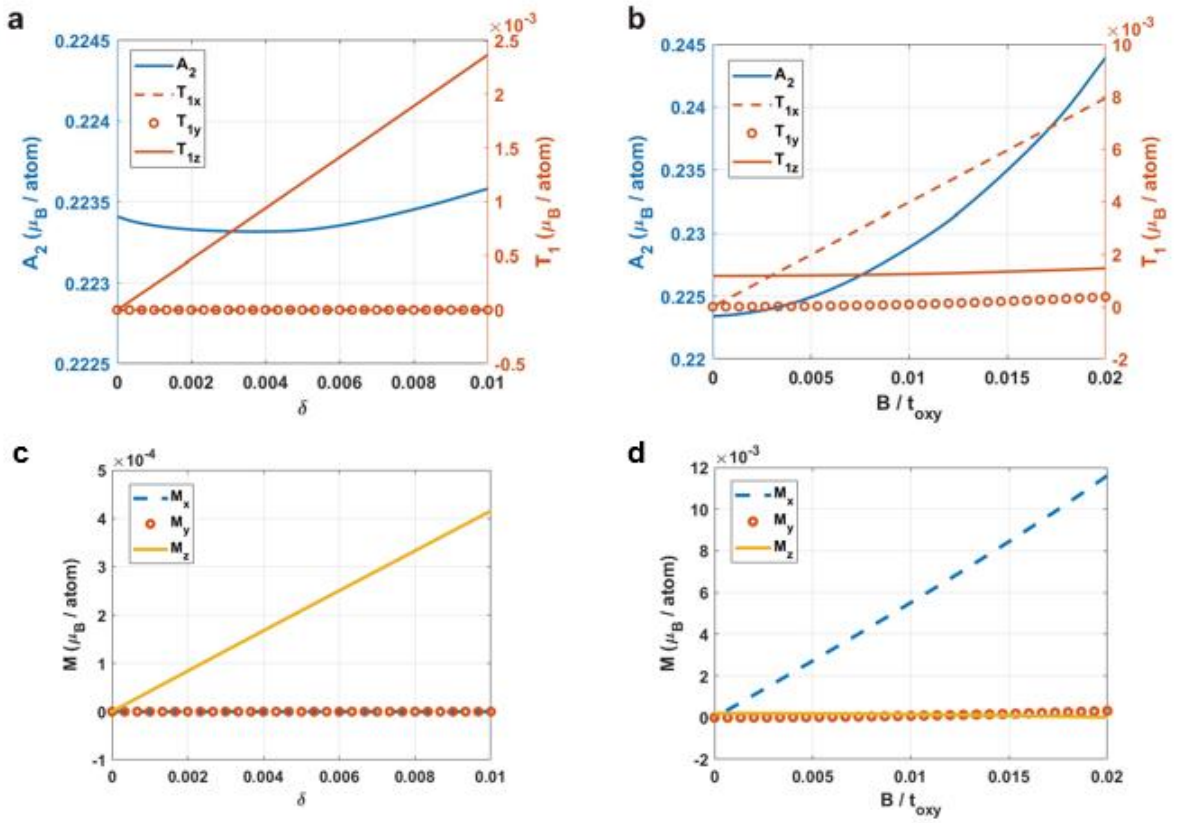

Figure 4.6 The emergence of T_1-octupole under strain and magnetic field. We present A_2-octupole and T_1-octupoles under the change of strain and magnetic field. The blue solid line is A_2, the orange dotted line is T_{1x}, the orange circles are T_{1y}, and the orange solid line is T_{1z}. a. The change of order parameters when the strain δ varies from 0 to 0.01 with $\vec{B} = 0$. When the strain is absent ($\delta = 0$), only A_2-octupole exists. When $\delta \neq 0$, only T_{1z} emerges linearly to δ while T_{1x} and T_{1y} remains trivial. b. The change of order parameters when magnetic field strength varies from 0 to 0.02 with $\phi = 0, \delta = 0.005$. T_{1x} emerges linearly to δ, and other order parameters change quadratically to δ. c. The change of magnetization when the strain δ varies from 0 to 0.01 with $\vec{B} = 0$. d. The change of magnetization when magnetic field strength varies from 0 to 0.02 with $\phi = 0, \delta = 0.005$.

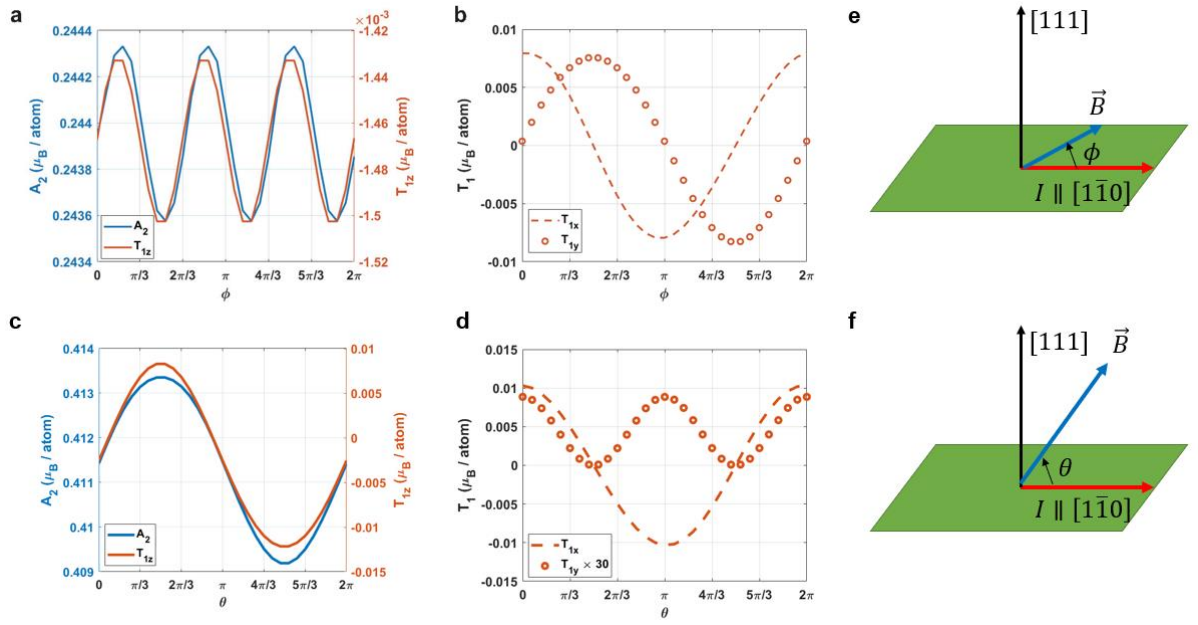

Figure 4.7 The angular dependence of A_2 and T_1-octupoles. We present the change of order parameters for two cases. a-b. $\vec{B}$ is in the [111] plane. ϕ varies from 0 to 2π, with $\delta = 0.005, U = 1.485\, t_{oxy}$, and $B = 0.02$. a. A_2-octupole (blue solid line) and T_{1z}-octupole (orange solid line) which are proportional to $sin\, 3\phi$. b. T_{1x} (orange dotted line) and T_{1y} (orange circles) which are proportional to $cos\, \phi$ and $sin\, \phi$, respectively. c-d. $\vec{B}$ is in the $[11\bar{2}]$ plane. θ varies from 0 to 2π, with $\delta = 0.01, U = 1.5\, t_{oxy}$, and $B = 0.02$. c. A_2-octupole (blue solid line) and T_{1z}-octupole (orange solid line) are proportional to $sin\, 3\theta$. d. T_{1x} (orange dotted line) and 30 times T_{1y} (orange circles) which are proportional to $cos\, \theta$ and $cos\, 2\theta$, respectively. The schematics of the physical geometry when e. $\vec{B}$ in the [111] plane and f. $\vec{B}$ in the $[11\bar{2}]$ plane.

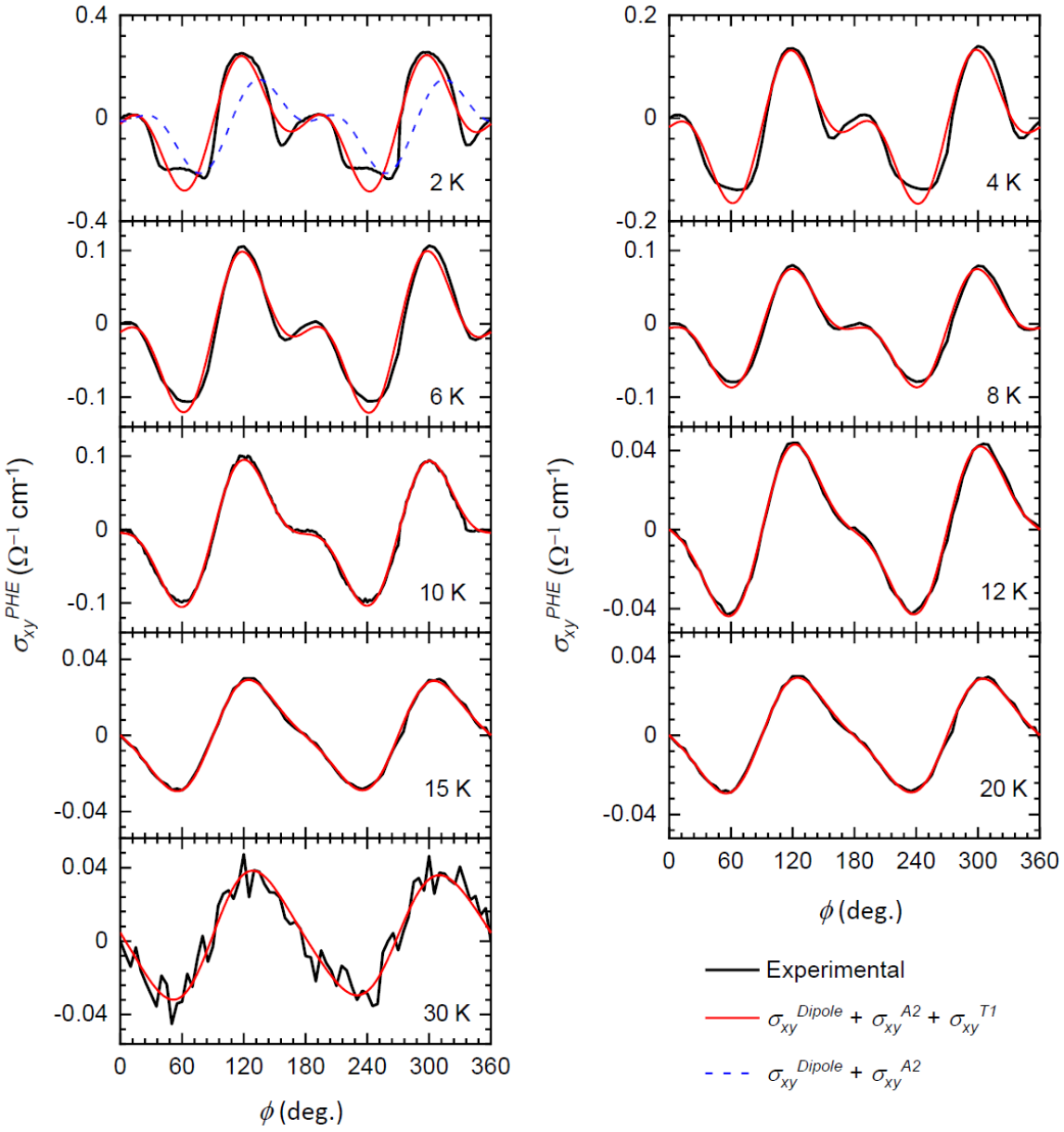

Figure 4.8 Plot of the calculated PHC below 30 K and their fitting results.

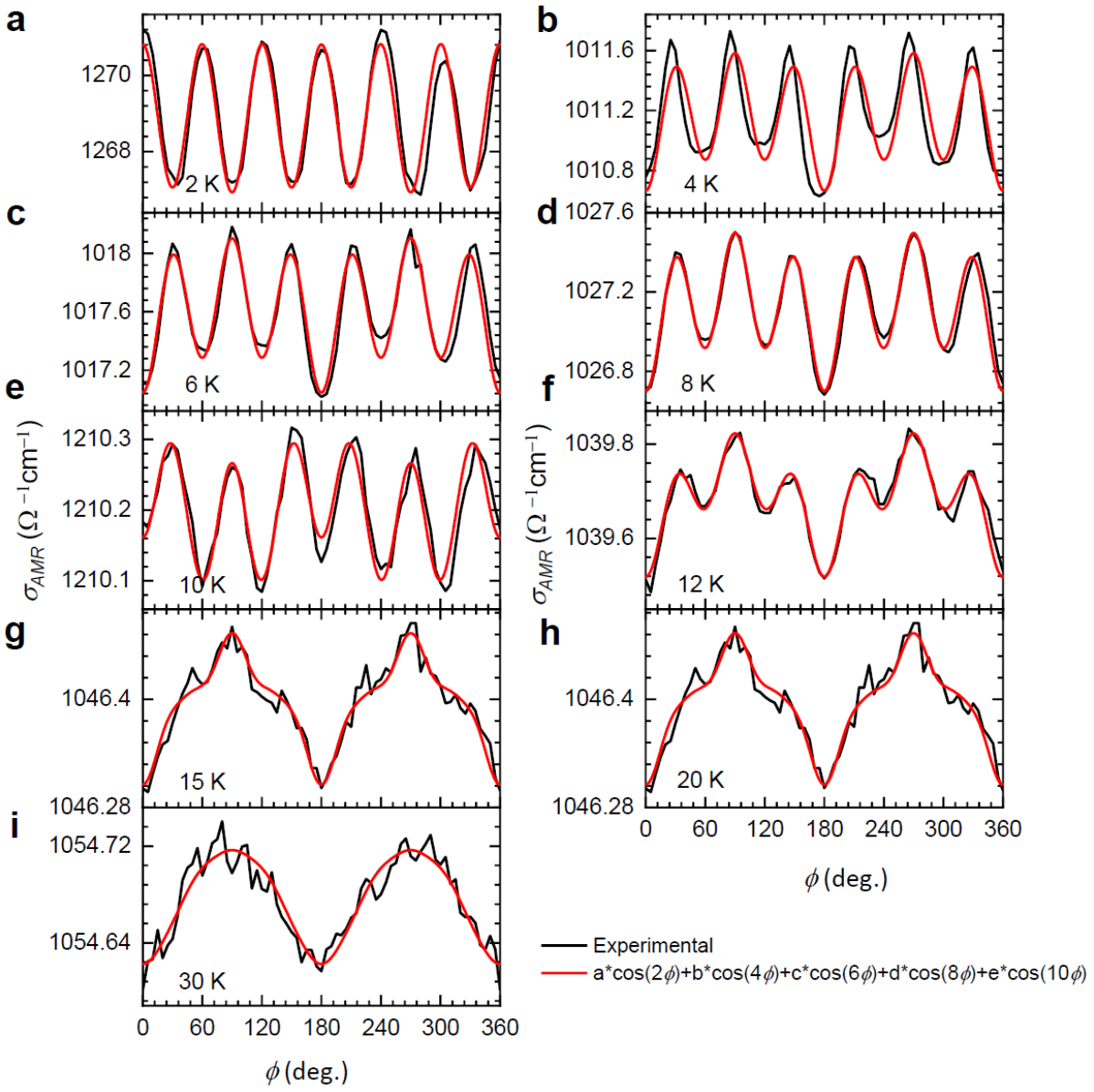

Figure 4.9 Anisotropic magnetoconductance and fitting with cluster multipoles contributions. σ_{AMR} (ϕ) measured at a. 2 K, b. 4 K, c. 6 K, d. 8 K, e. 10 K, f. 12 K, g. 15 K, h. 20, and i. 30 K. The black line is experimental data while the red line is the fitting result with theoretical AMR equation.

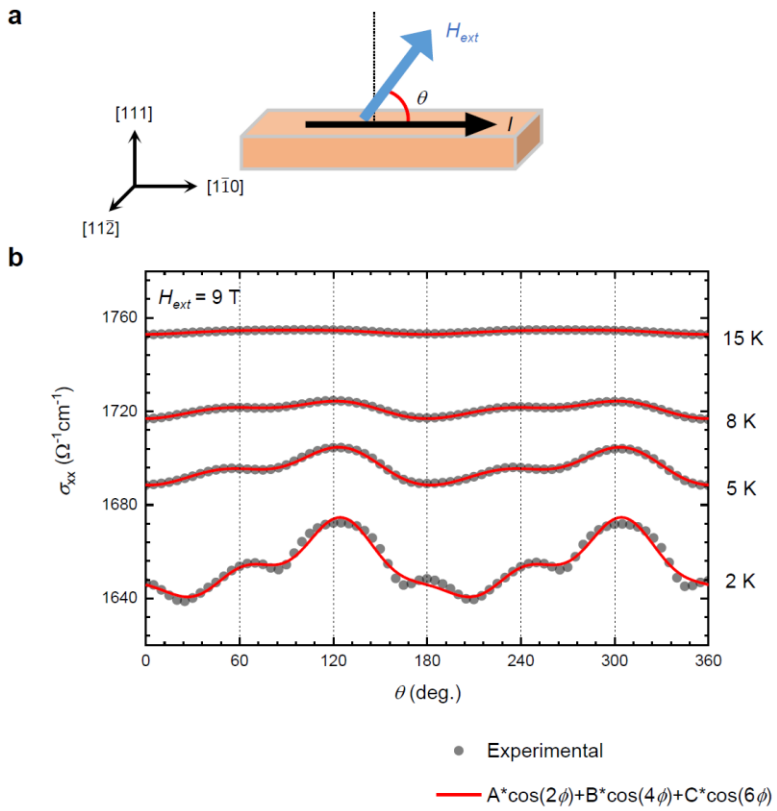

Figure 4.10 Temperature dependence of out-of-plane rotation magnetoconductivities. a. Schematic of out-of-plane rotation measurement. The current is applied along [1$\bar{1}$0] direction and magnetic field is rotated along [111] and [1$\bar{1}$0] plane. b. Experimental magnetoconductivities below 15 K and their fitting.

4.4 Conclusion

In summary, the PHE of the AFM NIO-227 film exhibits unique features different from those of ferromagnetic materials. The CMOs without magnetization affect the PHE, resulting in higher harmonics of the PHE oscillation beyond the second harmonic. Notably, A_2- and T_1-CMOs produce fourth and sixth harmonics of PHE oscillations, respectively. This feature of CMOs can be well explained by considering the magnetic characteristic of CMOs called OM in our theoretical calculations. Moreover, the OM of CMOs shows an intriguing H_{ext} dependency, which induces the nonlinear PHE when the angle between H_{ext} and I is 45°.

We want to make some remarks about the CMOs in AFM materials. According to recent theoretical studies and experiments on antiferromagnets, the magnetic octupole is crucial for stabilizing Weyl fermions near the Fermi energy[18,27,47-51] and inventing magnetic field-free switching spintronic devices[23-25, 48-50]. Moreover, AHE, SHE, and Nernst effects have been experimentally observed in kagome antiferromagnets[19-20,25-26,29], in which magnetic structure can also be classified with CMO[18]. Therefore, understanding and manipulating the CMOs are thus important to achieve novel topological phases and physics in AFM systems. However, due to the absence of magnetization, the detection and characterization of CMOs and multipoles beyond dipoles have been difficult. In this context, our strategy to distinguish A_2- and T_1-CMOs could be extensively used to detect and identify cluster multipoles[18,45] via the PHE. Thus, our work paves the way for detecting and identifying AFM order, which is expected to facilitate the development of novel functionalities using AFM materials.

References

1. Shick, A. B. et al. Spin–orbit coupling induced anisotropy effects in bimetallic antiferromagnets: A route towards antiferromagnetic spintronics. *Phys. Rev. B* **81**, 212409 (2010).
2. MacDonald, A. H. & Tsoi, M. Antiferromagnetic metal spintronics. *Phil. Trans. R. Soc. A* **369**, 3098–3114 (2011).
3. Gomonay, E. V. & Loktev, V. M. Spintronics of antiferromagnetic systems. *Low Temp. Phys.* **40**, 17–35 (2014).
4. Gomonay O., Jungwirth, T. & Sinova, J. Concepts of antiferromagnetic spintronics. *Phys. Stat. Sol. RRL*. **11**, 1700022 (2017).
5. Jungwirth T., Marti, X., Wadley, P. & Wunderlich, J. Antiferromagnetic spintronics. *Nat. Nanotechnol.* **11**, 231–241 (2016).
6. Wan, X., Turner, A. M., Vishwanath, A. & Savrasov, S. Y. Topological semimetal and Fermi-arc surface states in the electronic structure of pyrochlore iridates. *Phys. Rev. B* **83**, 205101 (2011).
7. Burkov, AA. & Balents L. Weyl Semimetal in a Topological Insulator Multilayer. *Phys. Rev. Lett.* **107**(12), 127205 (2011).
8. Liu, D. F. et al. Magnetic Weyl semimetal phase in a Kagomé crystal. *Science* **365**, 1282–85 (2019).
9. Li, J. et al. Intrinsic magnetic topological insulators in van der Waals layered $MnBi_2Te_4$-family materials. *Sci. Adv.* **5**, eaaw5685 (2019).
10. Varnava, N. & Vanderbilt, D. Surfaces of axion insulators. *Phys. Rev. B* **98**, 245117 (2018).
11. Zhang, R.-X., Wu, F. & Sarma. S. D. "Möbius insulator and higher-order topology in $MnBi_{2n}Te_{3n+1}$," *Phys. Rev. Lett.* **124**, 136407 (2020).
12. Marti, X. et al. Room-temperature antiferromagnetic memory resistor. *Nat. Mater.* **13**, 367–374 (2014).
13. Wadley, P. et al. Electrical switching of an antiferromagnet. *Science* **351**, 587–590 (2016).
14. Kirilyuk, A., Kimel, A. V. & Rasing, Th. Ultrafast optical manipulation of magnetic order. *Rev. Mod. Phys.* **82**, 2731–2784 (2010).

15. Tzschaschel, C. et al. Ultrafast optical excitation of coherent magnons in antiferromagnetic NiO. *Phys. Rev. B* **95**, 174407 (2017).

16. Kampfrath, T. et al. Coherent terahertz control of antiferromagnetic spin waves. *Nat. Photon.* **5**, 31–34 (2011).

17. Pashkin, A., Sell, A., Kampfrath, T. & Huber, R. Electric and magnetic terahertz nonlinearities resolved on the sub-cycle scale. *New J. Phys.* **15**, 065003 (2013).

18. Suzuki, M. T., Koretsune, T., Ochi, M. & Arita, R. Cluster multipole theory for anomalous Hall effect in antiferromagnets. *Phys. Rev. B* **95**, 094406 (2017).

19. Nayak, A. K. et. al. Large anomalous Hall effect driven by a nonvanishing Berry curvature in the noncolinear antiferromagnet. *Sci. Adv.* **e1501870** (2016).

20. Kiyohara, N. et al. Giant Anomalous Hall Effect in the Chiral Antiferromagnet Mn_3Ge. *Phys. Rev. Appl.* **5**, 064009 (2016).

21. Kim, W. J. et al. Strain engineering of the magnetic multipole moments and anomalous Hall effect in pyrochlore iridate thin films. *Sci. Adv.* **6** eabb1539 (2020).

22. Higo, T. et al. Large magneto-optical Kerr effect and imaging of magnetic octupole domains in an antiferromagnetic metal. *Nature Photon* **12**, 73–78 (2018).

23. Kimata, M., Chen, H., & Kondou, K. et al. Magnetic and magnetic inverse spin Hall effects in a non-collinear antiferromagnet. *Nature* **565,** 627–630 (2019).

24. Muduli, P. K. et al. Evaluation of spin diffusion length and spin Hall angle of the antiferromagnetic Weyl semimetal Mn_3Sn. *Phys. Rev. B* **99**(18), 184425 (2019).

25. Zhang, Y. et al. Strong anisotropic anomalous Hall effect and spin Hall effect in the chiral antiferromagnetic compounds Mn_3X (X = Ge, Sn, Ga, Ir, Rh, and Pt). *Phys. Rev. B* **95**, 075128 (2017)

26. Ikhlas, M. et al. Large anomalous Nernst effect at room temperature in a chiral antiferromagnet. *Nature Phys* **13,** 1085–1090 (2017).

27. Chen, T. et al. Anomalous transport due to Weyl fermions in the chiral antiferromagnets Mn_3X, X = Sn, Ge. *Nat. Commun.* **12**, 572 (2021).

28. Sakai, A. et al. Giant anomalous Nernst effect and quantum-critical scaling in a ferromagnetic semimetal. *Nat. Phys.* **14,** 1119–1124 (2018).

29. Broholm, C. et al. Antichiral spin order, its soft modes, and their hybridization with phonons in the topological semimetal Mn_3Ge. *Phys. Rev. B* **102,** 054403 (2020).

30. Liang, T. et al. Orthogonal magnetization and symmetry breaking in pyrochlore iridate $Eu_2Ir_2O_7$. *Nat. Phy.* **13**, 599-603 (2017).

31. Kimata, M. et al. X-ray study of ferroic octupole order producing anomalous Hall effect. *Nat Commun* **12,** 5582 (2021).

32. Zhou, J. et al. Large spin-orbit torque efficiency enhanced by magnetic structure of collinear antiferromagnet IrMn. *Sci. Adv.* **5** eaau6696 (2019).

33. Tang, H. X. et al. Giant planar Hall effect in Epitaxial (Ga, Mn) As devices. *Phys. Rev. Lett.* **90,** 107201 (2003).

34. Bowen, M. et al. Order-driven contribution to the planar Hall effect in Fe_3Si thin films. *Phys. Rev. B* **71,** 172401 (2005).

35. Ge, Z. et al. Magnetization reversal in (Ga, Mn) As/Mn O exchange-biased structures: Investigation by planar Hall effect. *Phys. Rev. B* **75,** 014407 (2007).

36. Bason, Y. et al. Giant planar Hall effect in colossal magnetoresistive $La_{0.84}Sr_{0.16}MnO_3$ thin films. *Appl. Phys. Lett.***84**, 2593 (2004).

37. Liang, D. et al. Origin of planar Hall effect in type-II Weyl semimetal $MoTe_2$, *AIP Adv.* **9**, 055015 (2019).

38. Yang, S. et al. Field-Modulated Anomalous Hall Conductivity and Planar Hall Effect in $Co_3Sn_2S_2$ Nanoflakes. *Nano Lett.* **20**, 7860-7867 (2020).

39. Li, P., et al. Giant planar Hall effect in the Dirac semimetal $ZrTe_{5-\delta}$, *Phy. Rev. B* **98**, 121108 (2018).

40. Burkov, AA, Giant planar Hall effect in topological metals, *Phys. Rev. B* **96**, 041110(R) (2017).

41. Li, Y. et al. Correlated Magnetic Weyl Semimetal State in Strained $Pr_2Ir_2O_7$. *Adv. Mat*. **33**, 2008528 (2021).

42. Huang, D. et al. Planar Hall effect with sixfold oscillations in a Dirac antiperovskite. *Phy. Rev. Research* **3**, 013268 (2021).

43. Neha, W. et al. Planar Hall effect and anisotropic magnetoresistance in the polar-polar interface of $LaVO_3$-$KTaO_3$ with strong spin-orbit coupling. *Nat. Comm.* **11**, 874. (2020).

44. Bhardwaj, A. et al. Observation of planar Hall effect in topological insulator—Bi_2Te_3. *Appl. Phys. Lett.* **118**, 241901 (2021).

45. Suzuki, M. T. et al. Multipole expansion for magnetic structures: A generation scheme for a symmetry-adapted orthonormal basis set in the crystallographic point group. *Phys. Rev. B* **99**, 174407 (2019)

46. Tian, Z. et al. Field-induced quantum metal-insulator transition in the pyrochlore iridate $Nd_2Ir_2O_7$. *Nat. Phys.* **12**, 134 (2016).

47. Kuroda, K. et al. Evidence for magnetic Weyl fermions in a correlated metal. *Nat. Mater.* **16**, 1090–1095 (2017).

48. Li, X. et al. Chiral domain walls of Mn_3Sn and their memory. *Nat Commun* **10,** 3021 (2019).

49. You, Y. et al. Cluster magnetic octupole induced out-of-plane spin polarization in antiperovskite antiferromagnet. *Nat Commun* **12,** 6524 (2021).

50. Xu, L. et al. Planar Hall effect caused by the memory of antiferromagnetic domain walls in Mn_3Ge *Appl. Phys. Lett.* **117**, 222403 (2020).

51. Witczak-Krempa, W., Go, A., & Kim, Y. B. Pyrochlore electrons under pressure, heat, and field: Shedding light on the iridates. *Phys. Rev. B* **87**, 155101 (2013).

List of Publication

1. "Oxygen Vacancy Engineering for Highly Tunable Ferromagnetic Properties: A Case of $SrRuO_3$ Ultrathin Film with a $SrTiO_3$ Capping Layer"

   Eun Kyo Ko, Junsik Mun, Han Gyeol Lee, Jinkwon Kim, **Jeongkeun Song**, Seo Hyoung Chang, Tae Heon Kim, Suk Bum Chung, Miyoung Kim, Lingfei Wang, Tae Won Noh
   Adv. Funct. Mat. **30**, 2001486 (2020).

2. "Strain engineering of the magnetic multipole moments and anomalous Hall effect in pyrochlore iridate thin films"

   Woo Jin Kim, Taekoo Oh, **Jeongkeun Song**, Eun Kyo Ko, Yangyang Li, Junsik Mun, Bongju Kim, Jaeseok Son, Zhuo Yang, Yoshimitsu Kohama, Miyoung Kim, Bohm-Jung Yang, Tae Won Noh
   Sci. adv. **6**, eabb1539 (2020).

3. "Correlated Magnetic Weyl Semimetal State in Strained $Pr_2Ir_2O_7$"

   Yangyang Li, Taekoo Oh, Jaeseok Son, **Jeongkeun Song**, Mi Kyung Kim, Dongjun Song, Sukhyun Kim, Seo Hyoung Chang, Changyoung Kim, Bohm-Jung Yang, Tae Won Noh
   Adv. Mat. **33**, 2008528 (2021).

4. "Perspective on solid-phase epitaxy as a method for searching novel topological phases in pyrochlore iridate thin films"

   Woo Jin Kim, **Jeongkeun Song**, Yangyang Li, Tae Won Noh
   APL Mater. **10**, 080901 (2022).

5. "Higher harmonics in planar Hall effect induced by cluster magnetic multipoles"

   Jeongkeun Song, Taekoo Oh, Eun Kyo Ko, Ji Hye Lee, Woo Jin Kim, Yangyu Zhu, Bohm-Jung Yang, Yangyang Li, and Tae Won Noh
   Nature Communications **13**, 6501 (2022).

6. "Tuning orbital-selective phase transitions in a two-dimensional Hund's correlated system"

   Eun Kyo Ko, Sungsoo Hahn, Changhee Sohn, Sangmin Lee, Seung-Sup B. Lee, Byungmin Sohn, Jeong Rae Kim, Jaeseok Son, **Jeongkeun Song**, Youngdo Kim, Donghan Kim, Miyoung Kim, Choong H. Kim, Changyoung Kim
   Accepted Nature Communications (2023).
7. "Extended oxygen octahedral tilt proximity near oxide heterostructures"

   Junsik Mun, Eun Kyo Ko, Baekjune Kang, Byeongjun Gil, Choong H. Kim, Sungsoo Hahn, **Jeongkeun Song**, Yimei Zhu, Changhee Sohn, Tae Won Noh, and Miyoung Kim
   Nano Lett. **23**, 1036-1043 (2023).

8. "Engineering Structural Homogenity and Magnetotransport in strained $Nd_2Ir_2O_7$ thin films"

   Jeongkeun Song, Jihwan Jeong, Eun Kyo Ko, Ji Hye Lee, Woo Jin Kim, Sangmin Lee, Miyoung Kim, Yangyang Li, Tae Won Noh.
   APL Materials **10,** 080901 (2023).

국문 초록 (Abstract in Korean)

밴드 토폴로지가 있는 양자 물질을 찾는 것은 재료과학 및 응집 물질 물리학 분야의 중심주제 중 하나였습니다. 5d 파이로클로로 이리듐 계열 ($R_2Ir_2O_7$, R = 희토류 이온) Coulomb 상호 작용(U) 및 스핀-궤도 결합(λ)과 같은 매개 변수의 비교 가능한 강도 간의 상호 작용으로 인해 상당한 관심을 받았습니다. 이 상호 작용은 토폴로지 절연체, 바일반금속 상태 및 액시온 절연체를 포함하여 물질의 비옥한 토폴로지 상태를 초래할 것으로 예측됩니다.

$R_2Ir_2O_7$박막은 입방체 결정 대칭으로 인해 대량으로 숨겨진 위상 위상 및 이국적인 현상을 조사하기에 적합한 플랫폼을 제공합니다. 에피택셜 변형은 입방정 결정 대칭을 깨뜨릴 수 있어 숨겨진 토폴로지 단계에 접근할 수 있는 실용적인 조정 가능성을 제공합니다. 광범위한 관심에도 불구하고 고품질 단결정(111) $R_2Ir_2O_7$박막의 제조는 성장 중에 고휘발성 기체 이리듐 산화물(IrO3)의 형성으로 인해 여전히 어려운 과제로 남아 있습니다. 성공적으로 성장된 $R_2Ir_2O_7$박막의 대부분은 "고상 에피택시(SPE)"라고 하는 2단계 프로토콜을 통해 실현되었습니다. 그러나 SPE 방법은 느슨하거나 부분적으로 변형된 $R_2Ir_2O_7$필름을 생성하므로 변형 유도 토폴로지 현상을 조사하는 데 적합하지 않습니다. 본 논문에서는 변형된 $Nd_2Ir_2O_7$(NIO-227) 박막 제조를 위한 새로운 성장 방법, 새로운 성장 방법을 최적화하고 활용하는 방법, 변형된 NIO-227 박막에서 변형 유도 자기수송 현상에 대해 논의할 것이다.

주요어: 위상적 상태, 파이로클로로 이리듐, 에피택셜 변형, 새로운 성장 방법, 자기수송.
학생번호: 2017-26221